REVERSE-TIME MIGRATION OF A METHANE GAS HYDRATE DISTRIBUTED ACOUSTIC

SENSING THREE-DIMENSIONAL VERTICAL SEISMIC PROFILE DATASET

by

Cullen I. Young

A thesis submitted to the Faculty and the Board of Trustees of the Colorado School of Mines in partial fulfillment of the requirements for the degree of Master of Science (Engineering Systems).

Golden, Colorado

Date _____

Signed: _____

Cullen I. Young

Signed: _____

Dr. Jeffrey C. Shragge
Thesis Advisor

Golden, Colorado

Date _____

Signed: _____

Dr. Paul Sava
Department Head Title
Department of Geophysics

ABSTRACT

Distributed acoustic sensing (DAS) has emerged as an important technology for seismic investigations for downhole vertical seismic profile (VSP) surveying. DAS fiber has high spatial and temporal resolution resulting in higher-quality and finely sampled P- and S- wavefields which motivates the development and refinement of a three-dimensional (3-D) seismic imaging framework capable of realizing the full potential of DAS data for generating high-resolution images of subsurface geological structure. The work reported in this thesis outlines the development and application of a full-wavefield seismic imaging framework using an acoustic reverse-time migration (RTM) procedure adapted from more standard surface-based seismic usage. The key advantages of using an RTM imaging procedure over other seismic imaging methods is in its ability to handle complex earth models, sharp velocity contrasts, and significant structural dips. The procedure was developed using synthetic velocity models and data, with imaging challenges (i.e., irregular surface topography, borehole deviations, and modeling frequencies to 100 Hz) examined prior to working with field data. The framework was then applied to a DAS 3-D VSP data set acquired on the North Slope of Alaska as part of a multi-partner methane-gas hydrate investigation. Preprocessing was conducted to isolate and improve the signal-to-noise ratio of compressional-wave (P-wave) data components that are used in the acoustic RTM framework. In addition, velocity model refinement was conducted to produce an accurate 3-D P-wave model required for RTM imaging. The 3-D RTM code, utilizing graphical processing units for faster wavefield computations, was used to develop high-quality images of the two target hydrate sand reservoirs. The overall work shows that using a high-frequency 3-D RTM imaging procedure with DAS 3-D VSP data results in high-quality and interpretable subsurface images, which were validated through an accurate well-tie analysis. Suggested future research activities include development of more advanced inversion approaches (e.g., acoustic or elastic least-squares RTM) that could generate higher-resolution images and lead to more quantitative subsurface reflectivity estimates allowing for better geologic interpretation and understanding of target hydrate reservoirs.

TABLE OF CONTENTS

LIST OF FIGURES

LIST OF ABBREVIATIONS

Acoustic Wave Equation . . . . AWE

Base of Ice Bearing Permafrost . . . . BIBPF

Base of Significant Ice Bearing Permafrost . . . . BSIBPF

Centered in Time, Centered in Space . . . . CTCS

Colorado School of Mines . . . . CSM

Common Reflection Point . . . . CRP

Distributed Acoustic Sensing . . . . DAS

Elastic Full Waveform Inversion . . . . E-FWI

Finite Difference Time Domain . . . . FDTD

Graphics Processing Unit . . . . GPU

Least Squares Reverse Time Migration . . . . LSRTM

Logging While Drilling . . . . LWD

Normal Moveout . . . . NMO

Reverse Time Migration . . . . RTM

Stratigraphic Test Well . . . . STW

Three-Dimensional 3-D

Time Reverse Imaging . . . . TRI

True Vertical Depth . . . . TVD

Vertical Seismic Profiling . . . . VSP

ACKNOWLEDGMENTS

For those that shall follow after.

CHAPTER 1

INTRODUCTION

Seismic imaging and monitoring are important applications for understanding the baseline geology of an area of interest and for constraining any changes in subsurface properties over time. Seismic imaging is commonly used for generating 2-D or 3-D subsurface reflectivity images to characterize and facilitate interpretation of localized geologic structure and stratigraphy. Seismic monitoring is used in different scenarios to variably provide time-lapse (i.e., 4-D) images of subsurface change, or to ensure safety of the subsurface activities such as wastewater disposal. In hydraulic fracturing, imaging and monitoring are used to understand fracture locations and orientations with the associated safety considerations [1]. Similarly, 4-D monitoring is used in mining applications to help avoid blowouts and to better understand mine stability [2]. Seismic imaging and monitoring technologies are also used in carbon capture, utilization, and storage (CCUS) to understand the spatial saturation distribution of injected CO_2 and to evaluate CO_2 plume expansion [3].

Developments in seismic acquisition hardware and computing processing capabilities have generated increasing interest in more localized high-resolution seismic investigations for subsurface imaging and monitoring purposes. Conventional active-source seismic surveying can be done with either surface-based source and receiver acquisition or downhole vertical seismic profiling (VSP) using surface sources and downhole receivers. A key advantage of VSP surveying over surface-based studies is an ability to record higher-frequency data because the excited source wavefields largely transit one way from surface to the receivers in the well, thereby having shorter overall paths along which to experience higher-frequency attenuation. However, three major disadvantages of VSPs over surface-based surveys are: (1) the costs associated with drilling a well; (2) the associated limited spatial coverage from the fixed downhole receiver geometry; and (3) the challenge of measuring the downgoing wavefields with sufficient geophone spatial density (i.e., at 5 m or less).

Over the past decade, distributed acoustic sensing (DAS) has emerged as an important technology for seismic investigations [4–6]. Applications of DAS sensing systems require two essential components: (1) a deployed optical fiber cable that is ideally elastically coupled to the recording surface (well, earth surface, etc.); and (2) an interrogator unit (IU) that emits short laser pulses along the fiber and detects the light energy backscattered from minor heterogeneities within the fiber [7]. When an optical fiber is completely stationary, the IU measures zero temporal phase shift within the detected backscattered signal; however, when a fiber is strained by, e.g., a passing seismic wave, the small deformations associated with the wave

1

disturbance lead to phase shifts in the backscattered signal that the IU measures as a seismic data-like quantity, usually in a strain-rate format.

Combining a DAS IU system with downhole fiber deployment is increasingly being used as a tool for localized 3-D seismic investigations or for 4-D seismic monitoring activities [8]. The key reason behind these trends is that DAS fiber deployments provide dense receiver measurements along the length of a well (i.e., at the 1.0 m scale), which demonstrably leads to improvement in the resolution of seismic images[9]; however, images still have limited spatial extent due to the restricted aperture afforded by the source-receiver geometry. Having high spatial and temporal resolution allows for DAS system to record high-quality and finely sampled P- and S- wavefields with full elastic behavior. Additionally, using downhole DAS fibers that have been strapped to the outside of the well casings and cemented in place allows for repeat (4-D) seismic monitoring to be conducted at a reduced overall cost compared to conventional wireline deployed geophone systems. Using DAS fiber in downhole acquisition has proven to be successful in examples of microseismic event imaging and others [10, 11]. While DAS provides an opportunity for continuous dense seismic acquisition, it has drawbacks in terms of large data volumes and it only measures an along-fiber strain-rate quantity, which leads to challenges associated with broadside sensitivity, specifically measuring strain-rate data for wave disturbances arriving obliquely to the fiber [12].

Given the high-frequency and high-wavenumber content of acquired DAS 3-D VSP data, it is important to use seismic imaging methods that can take full advantage of such data characteristics. Therefore, developing a DAS 3-D VSP seismic imaging framework capable of producing high-resolution subsurface images and that can be adapted to other DAS 3-D VSP acquisition geometries is desirable. This thesis reports the development of such a 3-D full-wavefield acoustic seismic imaging framework based on conventional surface-based reverse-time migration (RTM) [13]. The RTM procedure uses an estimated source wavelet to forward propagate a source wavefield through a subsurface velocity model. It then injects preprocessed shot-gather data into the same model and propagates the results in reverse time as a receiver wavefield. Finally, correlating the propagating source and receiver wavefield using an imaging condition generates an individual shot image volume. A key requirement for stable propagation of high-frequency wavefields is that the velocity models through which waves propagate need to be sampled with a fine-scale discretization and wavefields must be recursively time-stepped at small time intervals. These sampling requirements lead to significant computational and memory complexity, which to date has led to limited use of high-frequency RTM (i.e., to 100 Hz) for most 3-D seismic imaging applications.

The past decade has seen an increased use of graphical processing units (GPUs) in 3-D seismic imaging studies. GPU cards have thousand of compute threads that can used to perform massively parallel computing tasks, including significantly accelerating 3-D RTM imaging [14]. In this work we develop a 3-D

GPU-based RTM code appropriate for DAS 3-D VSP geometries. In addition to hardware-derived computational speed-ups, we recognize that source-receiver reciprocity can be exploited to reduce the overall workload when the number of receivers is fewer than the number of source points. An additional feature of VSP geometries is that the RTM code must be able to handle receivers located in deviated well geometries and sources with an irregular distribution (e.g., VSP radial shot patterns). Finally, all of these RTM code features need to be tested on synthetic models and data to ensure the validity of the ensuing field imaging results.

1.1 Alaska DAS 3D VSP Case History

A key contribution presented in this thesis is demonstrating the value of the developed high-resolution acoustic RTM approach on a DAS 3-D VSP field data set acquired on an optical fiber installed at the Hydrate-01 stratigraphic test well (STW) drilled in the Prudhoe Bay Unit on the Alaskan North Slope. This project represents a collaboration among the Colorado School of Mines (CSM), US Department of Energy (DOE) National Energy Technology Laboratory (NETL), Japan Oil, Gas and Metals National Corporation (JOGMEC), and the U.S. Geological Survey (USGS). The Hydrate-01 borehole and other local and regional wells have confirmed the presence of regionally extensive gas-hydrate reservoir intervals beneath the approximately 2000 ft (600 m) thick regional permafrost layer. The two 40 ft (12 m) thick sand layers (D1 sand within regional unit D and B1 sand within unit B) hosting the gas hydrates deposits are interpretable from a regional 3-D surface seismic survey; however, higher-resolution images and finer geological details about the gas-hydrate system and minor near-borehole faulting were desired by the project team.

The DAS 3-D VSP data were acquired using a Vibroseis seismic energy source that utilizes a plate that vibrates the ground in a set multi-second "sweep" from low to high frequencies (2 to 200 Hz). Figure 1.1 shows the surface source locations and the downhole DAS fiber receivers. There are a total of 1701 surface shot locations that avoid pre-existing surface features such as a lakes, roads, and pingos. The borehole trajectory deviates in the NE direction with the fiber having a total of 994 receiver locations spaced every 3 ft (1.0 m), determined from a number of parameter considerations, including the refractive group index of the fiber, which are decided during the DAS data acquisition set up. The maximum source-wellhead offset of 3517 ft (1072 m) allows for a reasonable imaging aperture for undertaking full-wavefield RTM experiments.

Figure 1.2 shows DAS data examples for near, mid, and far source-receiver offsets. The dashed green line indicates the interpreted base of significant ice bearing permafrost (BSIBPF) [15], to the right of which the P- and S- wave velocities are inferred to significantly decrease due to the steepening moveout. The

3

near-offset gather data (Figure 1.2a-b) show clear downhole P-wave first arrivals (red curve) with a significant amount of upward-reflected energy (light blue curve). The mid-offset gather data (Figure 1.2c-d) have higher-amplitude direct S-wave arrivals (orange line) relative to the near-offset gather data as well as upward-reflected S-S waves (dark blue curve). The far-offset gather data (Figure 1.2e-f) have even stronger S-wave arrivals as well as significant P-S conversions (yellow curve) at depths below the interpreted BSIBPF. The overall increase in S-wave energy at father offsets is likely due to the combination of source radiation pattern as well as a more favorable angle-dependent sensitivity of the DAS recording system to high-angle S-wave polarizations. Overall, these examples show that the Alaskan DAS 3-D VSP data are high-quality, largely noise-free, and clearly exhibit a full range of expected full-wavefield elastic behavior. Given these attributes, applying RTM to this data set ideally should result in a high-quality DAS 3-D VSP case history where high-resolution subsurface RTM images can be produced and assist with ensuing geologic interpretation activities.
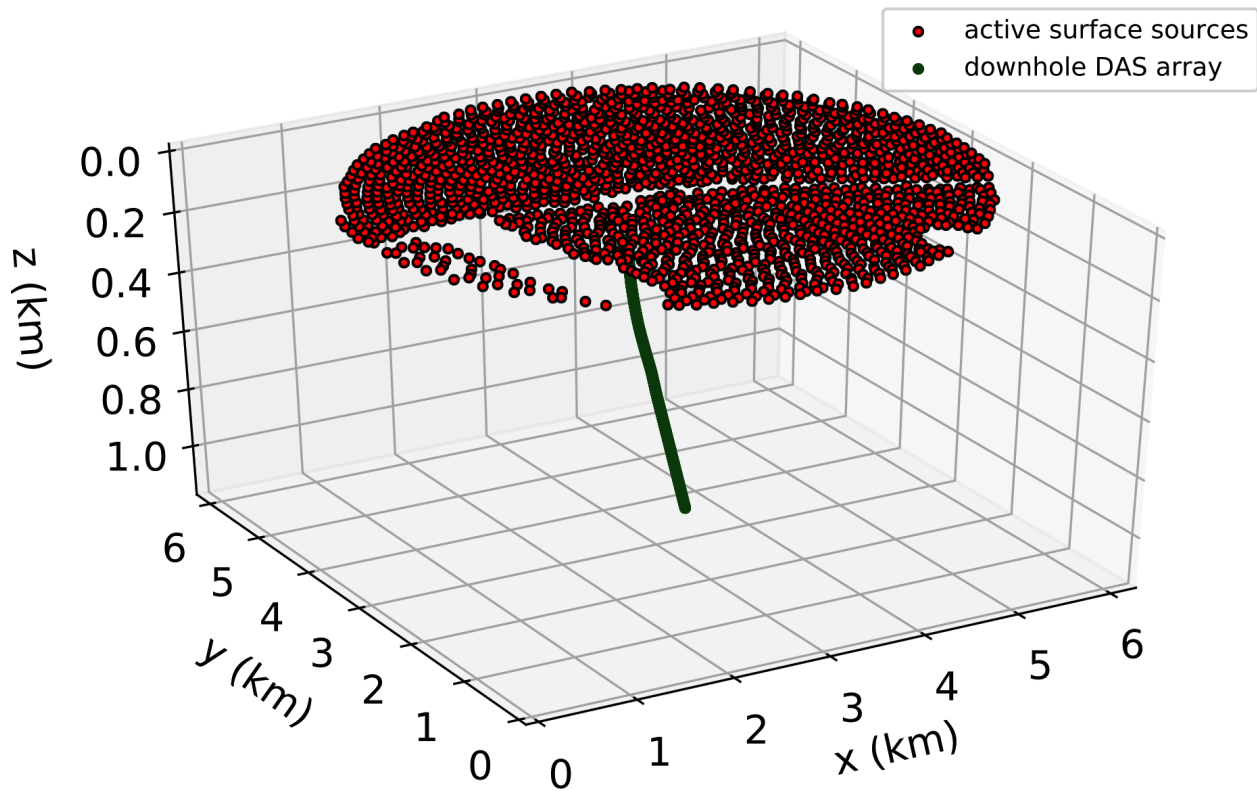
Figure 1.1 3D acquisition model showing surface source locations and DAS fiber receivers in the deviated borehole. There are a total of 1701 surface source locations while avoiding preexisting features such as a lakes, roads and pingos. The deviated borehole trajectory is in the NE direction with the fiber having a total of 994 receiver locations spaced every 3 ft (1.0 m).
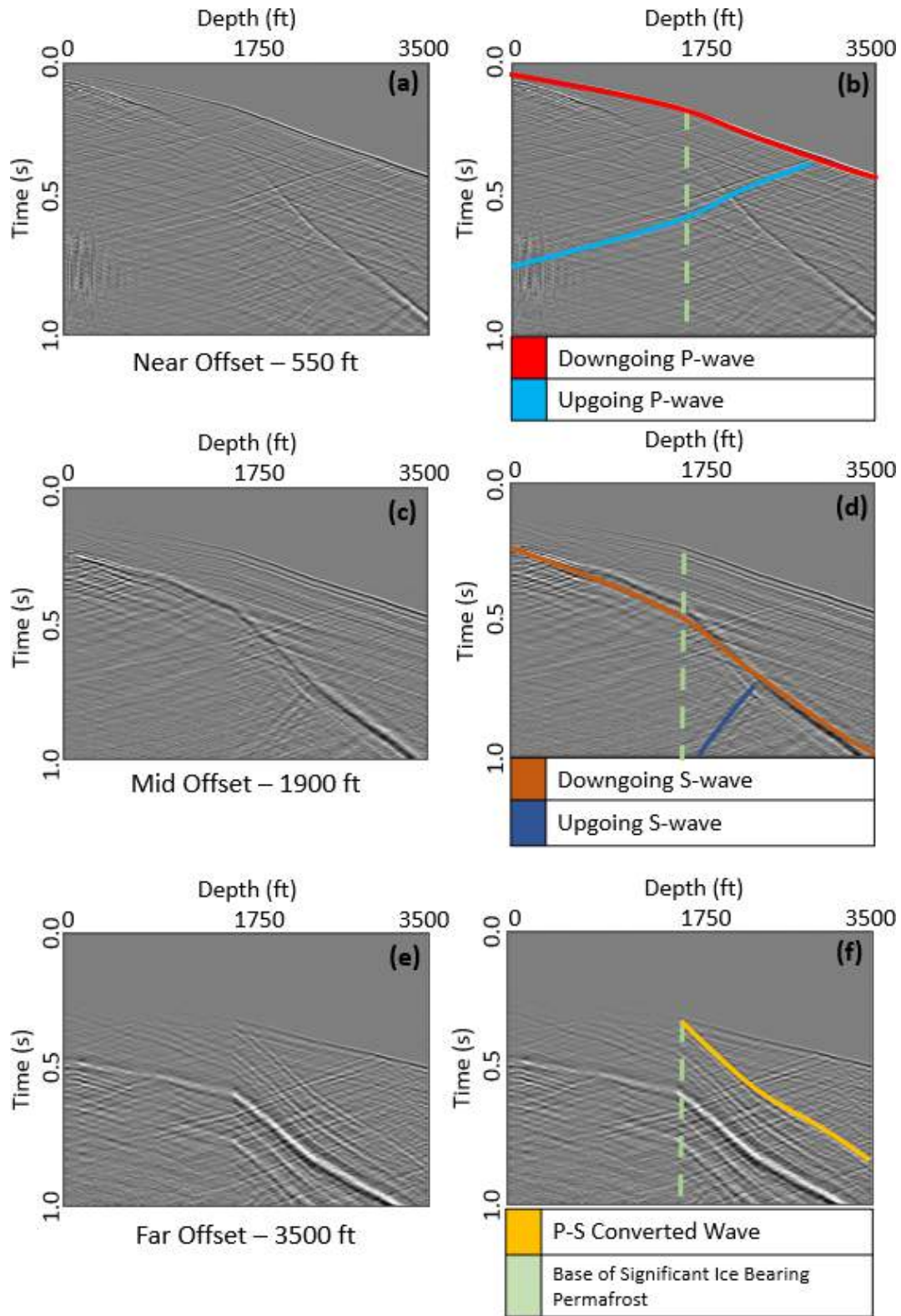
Figure 1.2 (a) Near-offset shot gather at 550 ft with (b) highlighting the direct P-wave arrivals and an example of an upgoing P-P reflection. (c) Mid-offset shot gather at 1900 ft with (d) marked direct S-wave arrivals and an example of an upgoing converted S-S reflection. (e) Far-offset shot gather at 3500 ft with (f) an example of a downgoing P-S conversion. The dashed green line represents the interpreted base of significant ice-bearing permafrost.

1.2 Thesis Outline

This thesis is split into four chapters, the first of which is the Introduction. Chapter 2 provides an overview of the 3-D acoustic RTM methodology and different imaging conditions used to generate final images. It then describes the particular RTM implementation, the synthetic data validation process, and additional considerations for handling the DAS 3-D VSP field data. Chapter 3 builds on the material presented in Chapter 2 by describing the full seismic imaging procedure applied to the gas hydrate DAS 3-D VSP data set. This includes the field data preprocessing, velocity model building and tomographic refinement, the application of RTM to the processed shot gathers, and analysis and discussion of the final results. This chapter was published in an Energy & Fuels special issue on studies associated with the Hydrate-01 STW [16]:

- Young, C., J. Shragge, W. Schultz, C. Oren, S. Haines, J. Simmons and T. Collett, 2022, Advanced Distributed Acoustic Sensing Vertical Seismic Profile Imaging of an Alaska North Slope Gas Hydrate Field: *Energy & Fuels*, **36**, no. 6. doi: https://doi.org/10.1021/acs.energyfuels.1c04102

Chapter 4 presents the overall project conclusions and discusses future research work that includes 3-D elastic imaging and inversion studies that would help researchers fully exploit the S-wave information clearly visible in the Alaska DAS 3-D VSP data set.

CHAPTER 2

REVERSE-TIME MIGRATION - THEORY AND GPU-BASED IMPLEMENTATION

Subsurface seismic imaging and 4-D seismic monitoring are fundamental methods for understanding the structure and stratigraphy of the local subsurface geology as well as for constraining changes in the associated physical properties over time. A common method used to generate seismic images is prestack depth migration (PSDM), which uses wavefield information propagated into the subsurface by solving the acoustic wave equation (AWE). While some seismic imaging methods involve approximate full wavefield solutions (including, among others, Kirchhoff [17] and Gaussian-beam [18] migration) and are used for their flexibility and efficiency, these methods are less effective for scenarios involving complex earth structure and models. Conversely, reverse time migration (RTM) is useful for higher-end seismic imaging scenarios involving complex earth models, significant structural dips, and sharp velocity contrasts [13]. RTM is a computationally expensive method compared with the lower-accuracy Kirchhoff and Gaussian Beam counterparts, and requires a significantly greater number of calculations to solve the full AWE. Recent improvements in computer hardware especially graphical processing units (GPUs), are making RTM analyses increasingly accessible for more general subsurface imaging applications.

2.1 RTM Overview

Unlike other more approximate PSDM methods, 3-D acoustic RTM explicitly solves the (usually constant-density) 3-D AWE given by:

$$\frac{\partial^2 U}{\partial t^2} = c^2 \left(\frac{\partial^2 U}{\partial x^2} + \frac{\partial^2 U}{\partial y^2} + \frac{\partial^2 U}{\partial z^2} \right), \tag{2.1}$$

where $\mathbf{x} = [x, y, z]$ are the three directional dimensions, t is time, $U(\mathbf{x}, t)$ is the acoustic wavefield, and $c(\mathbf{x})$ is the subsurface velocity distribution. RTM is termed a full-wavefield imaging method because it is not based on underlying approximation of the AWE like those used in Kirchhoff- or Gaussian beam-based migration. RTM exploits the time-reversal properties of the analytic AWE, meaning that acoustic wavefield solutions can be evolved either causally (forward) or anticausally (backward) in reverse time depending on context [13].

The acoustic RTM procedure has three fundamental steps. First, a seismic wavelet is injected into an initially quiescent source wavefield $S(\mathbf{x}, t)$ that is recursively numerically propagated forward in time from $t = 0$ s to a maximum recording time $t = T$ s. The second step involves injecting preprocessed P-wave reflection data to reconstruct a receiver wavefield $R(\mathbf{x}, t)$ which, along with the source wavefield solution,

are iteratively propagated in reverse time from $t = T$ s to $t = 0$ s. The third step involves applying an imaging condition that combines and stacks information from the $S(\mathbf{x}, t)$ and $R(\mathbf{x}, t)$ wavefields through a physical imaging condition on-the-fly at each time step in the reconstruction process (second step) to form a single-shot imaging volume. This three-step RTM imaging procedure is then repeated for each shot gather in the data set, with each successive image being stacked in to create the final global image volume.

2.1.1 Imaging Conditions

The third step in the RTM process involves applying an imaging condition to construct a 3-D image volume. Different approaches such as a standard zero-lag correlation or energy normalized imaging condition can be used resulting in different resolutions and illuminations in the image volume. A zero-lag correlation between the source S and receiver R wavefields is the most commonly applied RTM imaging condition:

$$I_C(\mathbf{x}) = \sum_e \sum_t S_e(\mathbf{x}, t) R_e(\mathbf{x}, t), \tag{2.2}$$

where e is the source index, and $I_C(\mathbf{x})$ represents the 3-D zero-correlation lag image volume. This imaging condition approach is fairly robust and straightforward to implement; however, in geologic scenarios with complex structures and strong impedance contrasts, the zero-lag correlation condition can generate low-wavenumber, high-amplitude artifacts.

To balance amplitudes and improve resolution one may use a energy normalized imaging condition [19], which is similar to the zero-lag correlation imaging condition in equation 2.2, but will focus on normalizing the source and receiver wavefields. A energy normalized imaging condition can be calculated via

$$I_D(\mathbf{x}) = \sum_e \sum_t \frac{S_e(\mathbf{x}, t) R_e(\mathbf{x}, t)}{\sqrt{S_e(\mathbf{x}, t)^2} \sqrt{R_e(\mathbf{x}, t)^2 + \epsilon^2}}, \tag{2.3}$$

where the stabilization factor ϵ is introduced to prevent division by zero, and $I_D(\mathbf{x})$ is the 3-D energy normalized volume. This imaging condition computes the zero-lag correlation between the source S and receiver R wavefields and normalizes the result by a measure of the energy present in the source and receiver wavefields to improve images by partially accounting for irregular illumination and imbalanced spectral frequency content. Care must be used to choose an ϵ value (usually through trial and error) that improves the spatial amplitude balance of reflectors but does not significantly increase imaging artifacts.

2.2 RTM Implementation

Having discussed the main components of the acoustic RTM procedure, I now present implementation details on simulating acoustic wavefield propagation and applying the imaging condition to produce a final image volume. This subsection presents the finite-difference (FD) stencil used to solve the 3D AWE along

with the source wavelet representation used in wavefield propagation. It also discusses the benefits of using GPU hardware and CUDA software implementation to improve efficiency. Using the GPU hardware, synthetic model development was conducted to generate a more complex velocity model input as well as testing the effects of the high-frequency source wavelet used in the experiments. Testing the acoustic RTM procedure on synthetic models assists with validating the final field data RTM results.

2.2.1 Generating Acoustic Wave Equation Solutions

The wavefield propagation calculation requires generating an AWE wavefield solution at each time step. In this work, I use a finite-difference time-domain (FDTD) solver with an temporal 2nd-order centered-in-time and spatial 8th-order centered-in-space (CTCS) stencil approximation of second-order partial derivatives found in equation 2.1. Figure 2.1 illustrates the 3-D spatial FD stencil geometry.
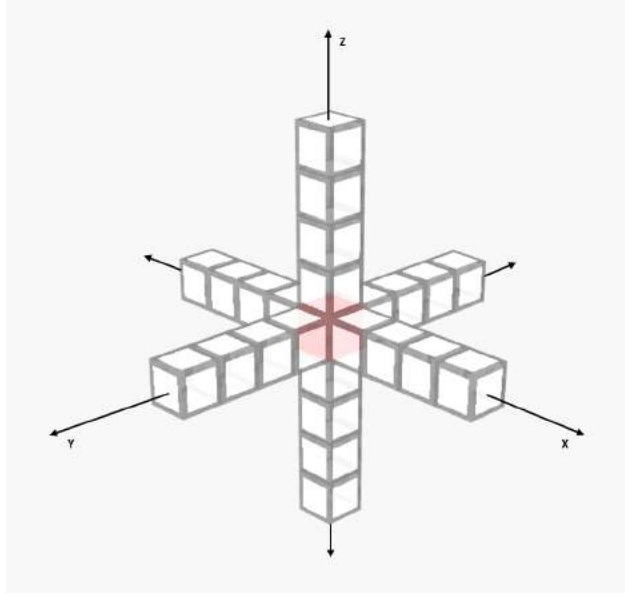
Figure 2.1 Illustration of the 25-point FD stencil used to propagated wavefields in the acoustic RTM procedure. The center red block indicates the calculated point, with transparent blocks indicating the points used to calculate the red block point.

Equation 2.4 gives the FD approximation including the FD stencil coefficients used in the wavefield propagation calculation,

$$U_{i,j,k}^{n+1} = 2U_{i,j,k}^n - U_{i,j,k}^{n-1} + \frac{\Delta t^2 c_{i,j,k}^2}{\Delta h^2} \sum_{n=-4}^{4} A_n(U_{i+n,j,k}^n + U_{i,j+n,k}^n + U_{i,j,k+n}^n), \tag{2.4}$$

where Δt and Δh are the temporal and uniform spatial discretization intervals, superscript n is the temporal index, $c_{i,j,k}$ is the velocity at the 3-D calculation point with subscripts i representing the x-axis, j the y-axis, and k the z-axis. Lastly, A_n is a vector of Taylor-series FD coefficients given by:

$$A_n = \left[-\frac{1}{560}, \frac{8}{315}, -\frac{1}{5}, \frac{8}{5}, -\frac{205}{72}, \frac{8}{5}, -\frac{1}{5}, \frac{8}{315}, -\frac{1}{560} \right], \quad n = -4, ..., 4.$$

When calculating the time-reversed wavefield propagation, the same FD approximations are used, but wavefield rotation allows for wavefield reversal.

To model the source wavefield we use a zero-phase Ormsby wavelet with [2, 8.5, 100, 150] Hz corner frequencies. The forward and reverse-time wavefield propagation involved 4000 time steps simulated at a $\Delta t = 0.3$ ms step interval which, given the spatial sampling and velocity model values, is sufficient to satisfy the Courant-Friedrichs-Lewy stability criteria [20]. Figure 2.2a presents the assumed Ormsby wavelet used to reproduce the source wavefield that produced the correlated Vibroseis data, while Figure 2.2b presents the associated frequency spectra that shows a flat response between approximately 10 Hz and 100 Hz.

(a)   (b)
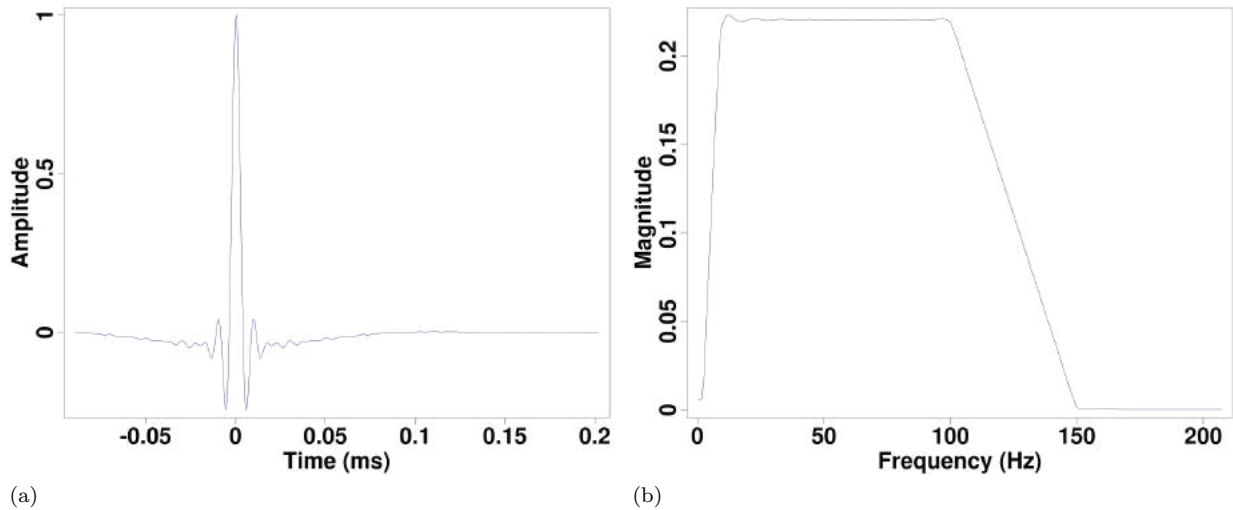
Figure 2.2 (a) Ormsby wavelet with [2, 8.5, 100, 150] Hz corner frequencies and (b) the corresponding frequency spectra used as the source wavelet in the RTM process.

Figure 2.3 shows four wavefield snapshots extracted as 2D slices of a 3D source wavefield volume in a homogeneous medium of P-wave velocity V_p=3.0 km/s using the aforementioned broadband Ormsby wavelet. The source wavelet was injected below the surface and injection location interpolated on to the grid using a linear inverse-distance weighting scheme. During the initial wavefield propagation tests, absorbing boundary conditions were not implemented at the computational domain boundaries, generating a free-surface reflection with -1 reflection coefficient that similarly propagates through the constant velocity model. Note the minimal numerical dispersion even though the source wavefield contained frequencies to 100 Hz.
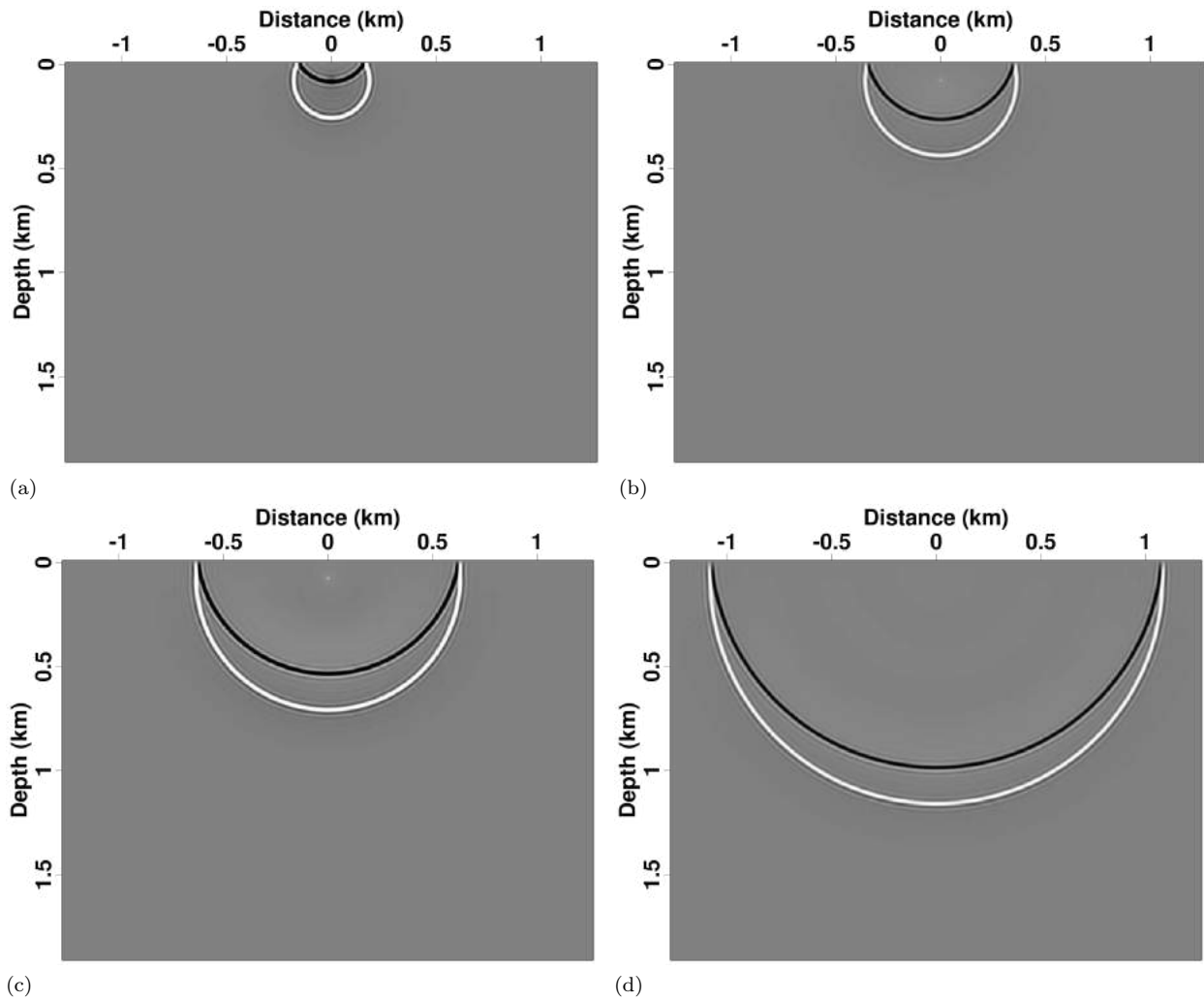
Figure 2.3 Source wavefield propagation using an Ormsby wavelet through a homogeneous velocity model. Snapshots shows at time steps: (a) $t = 0.24$ s, (b) $t = 0.39$ s, (c) $t = 0.54$ s, and (d) $t = 0.84$ s. Absorbing boundary conditions were not applied at the free surface, which leads to a free-surface multiple reflection with -1 reflection coefficient that similarly propagates through the constant velocity model.

2.2.2 GPU Implementation

Generating highly accurate source and receiver wavefields is a fundamental requirement for the RTM process to deliver high-quality images; however, developing an optimized RTM code and an efficient 3-D imaging process can be challenging due to the large number of surface sources and downhole receivers as well as the high-frequency modeling requirements. Our first approach for reducing the overall workload was to invoke principle of reciprocity [21], which is to exchange the source and receiver position locations, to decrease the number of sources needed for wavefield data injection. A second area of optimization was accelerating the efficiency of wavefield calculations. The FDTD AWE solver was optimized to run on

NVidia V100 GPU hardware using CUDA-based code, which can exploit the memory hierarchy and parallelism afforded by the GPU design. The GPU hardware allows users to achieve relatively fast and low-latency memory access between the compute cores and the stored wavefield values required for the required FD stencil calculations. Relative to the earlier and not well optimized CPU implementations of the same wavefield modeling operators, using the CUDA-based RTM code and GPU hardware resulted in a $20\times$ speedup. Given the four GPU cards contained within a single GPU cluster node, an additional benefit was the ability to concurrently calculate four individual shot gather images and thereby achieve an additional $4\times$ speedup.

2.2.3   Synthetic Model Development

The basic RTM code was developed and tested using homogeneous models for the purpose of validating the source and receiver wavefield propagation; however, additional code refinements need to be implemented prior to testing the RTM imaging process on field data. To address this, I developed a more complex 3-D synthetic model based on the field data observations reported in Chapter 3. This helped to ensure that key synthetic reflectors appeared at the approximate true estimated depths, and to help hone our expectations on what likely would be imaged in the field data.

As part of the larger Hydrate-01 stratigraphic test well project, logging while drilling (LWD) data were acquired with a group collaboration among the DOE-NETL, JOGMEC, and the USGS (see Figure 2.4). To generate a 3-D earth model, I read the processed LWD data into the Petrel [22] software package to generate an initial layered velocity model that could be used for modeling synthetic seismic data to help validate the 3-D RTM code and imaging procedure. Petrel has the capability to pick horizons from the data and upscale the petrophysical values into a 3-D model. A number of horizons initially were chosen for the primary targets, including the top of the well, the base of the well, the base of significant ice bearing permafrost, the base of ice bearing permafrost, the top and bottom of the D1 sand reservoir, and the top and bottom of the B1 sand reservoir. The complete 3D model, with upscaled petrophysical values, was then exported into a *.segy file format for initial RTM code development.

Figure 2.4 shows well log tracks read into the Petrel software system. Tracks are shown with depth in meters and titles from left to right include: PR: Poisson's ratio; ROBB: bulk density; VPVS: compressional to shear-wave velocity ratio; DTCO-MH-R: compressional-wave slowness; and Vp: calculated compressional-wave velocity. From observations within the data and target depths known, target horizons were selected, and petrophysical values upscaled for the particular horizon. Figure 2.5 illustrates the generated 3D model based on the selected well log horizon data. This model is for the Vp data, but similar models were generated for the Vs and density (ROBB) models. The Vp and Vs data were calculated from

the Vp and Vp/Vs slowness ratio well log to isolate the individual well logs.
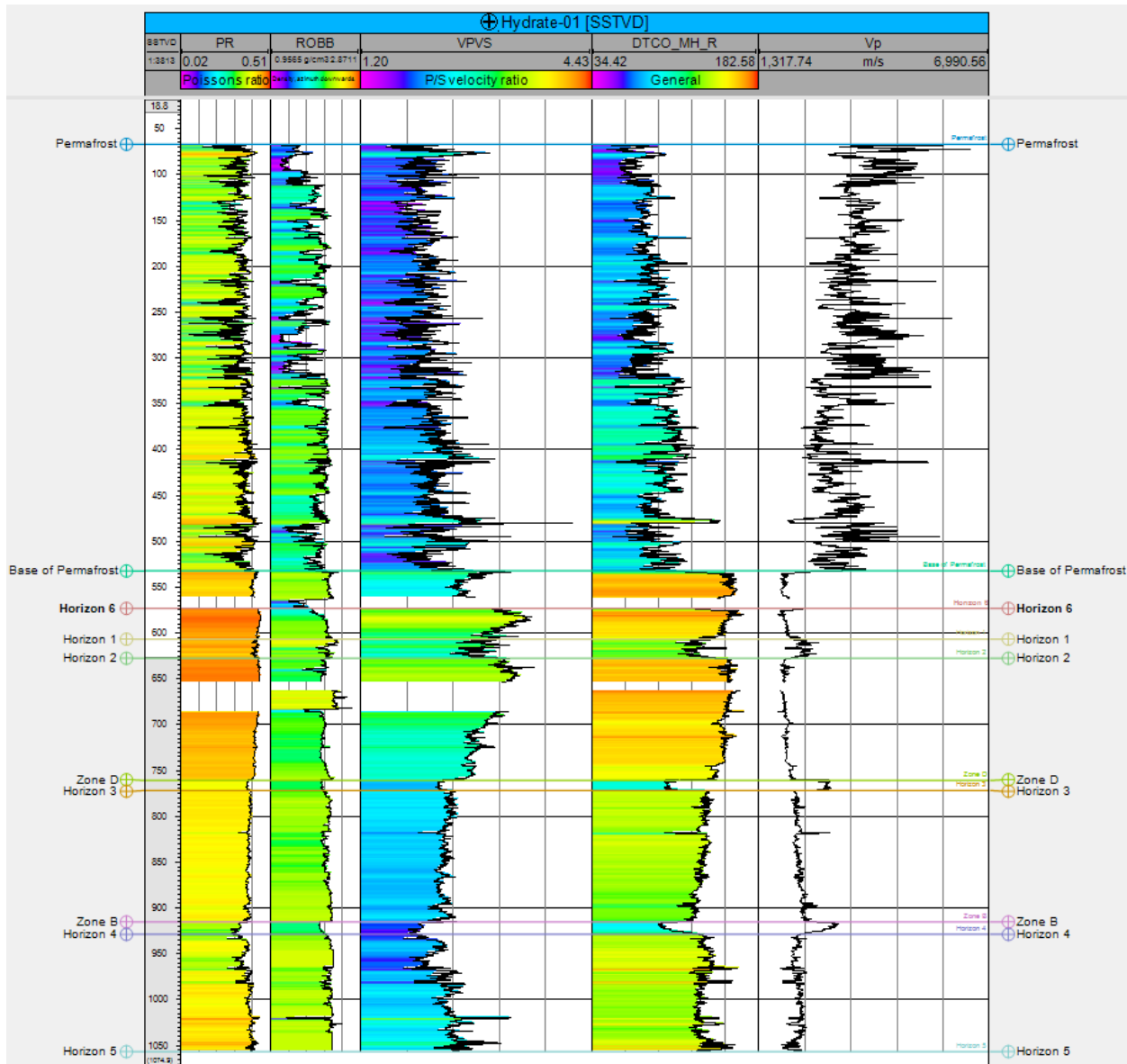
Figure 2.4 LWD data from the Hydrate-01 stratigraphic test well as visualized through Petrel. Tracks are shown with depth in meters and titles from left to right include: PR: Poisson's Ratio; ROBB: Bulk Density; VPVS: Compressional to Shear Velocity Ratio; DTCO-MH-R: Compressional Slowness; Vp: Calculated Compressional Velocity. Selected model horizons included the base of significant ice bearing permafrost, the base of ice bearing permafrost, the D1 hydrate sand reservoir and the B1 hydrate sand reservoir (see annotations to the right of the figure).
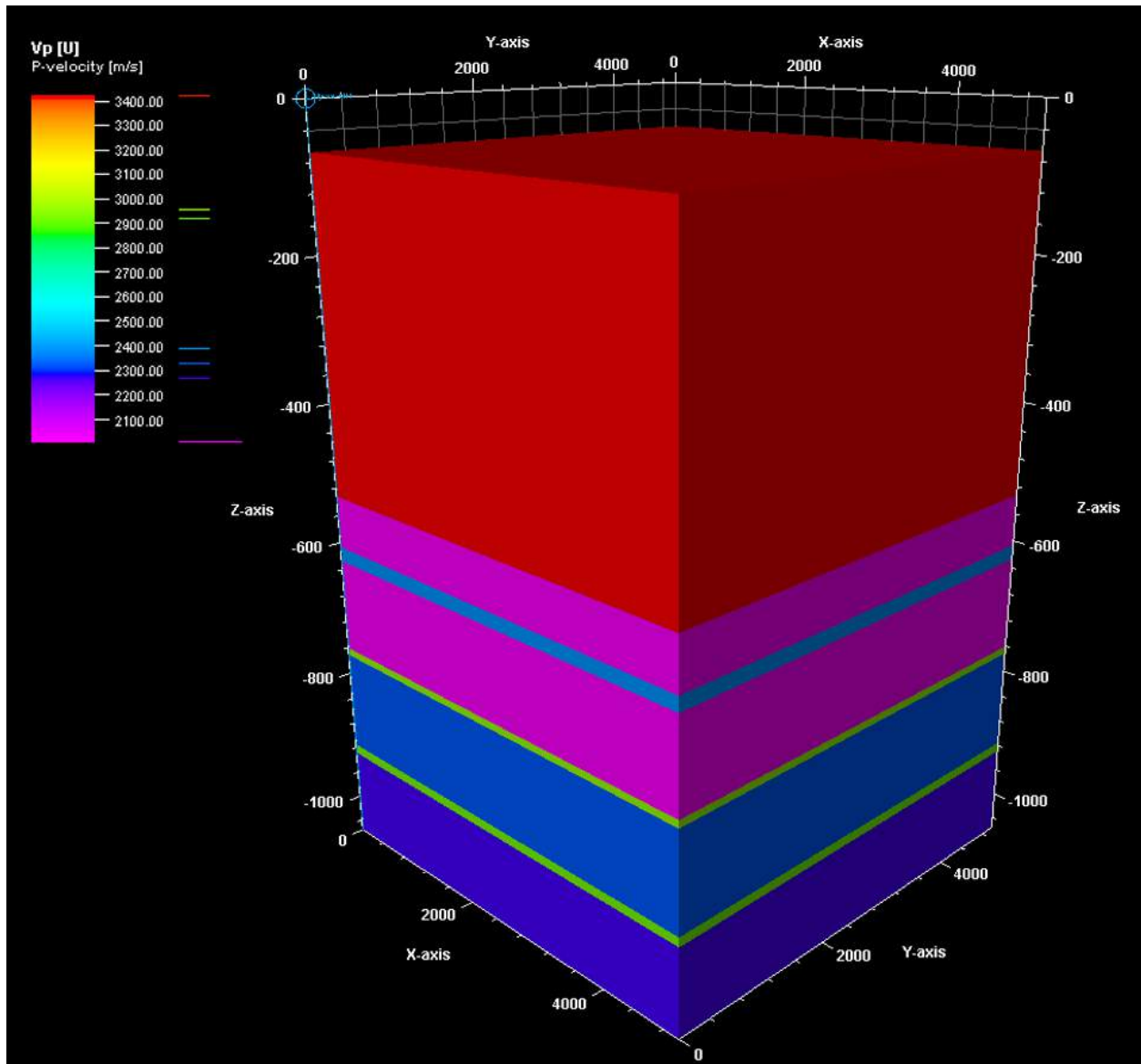
Figure 2.5 A 3D P-wave velocity (Vp) model with values upscaled from selected well log horizon data. Similar models were generated for the S-wave velocity (Vs) and density fields. Selected model horizons included the base of significant ice bearing permafrost, the base of ice bearing permafrost, the D1 hydrate sand reservoir and the B1 hydrate sand reservoir (see corresponding locations in Figure 2.4).

I then read the exported *.segy into the Madagascar software package, which was used to complete the acoustic 3-D RTM imaging process. Using the larger layered model developed in Petrel as a roughly synthetic model, assisted with testing and development of the RTM code and for determining the effectiveness of the RTM process in identifying the chosen key reflector units. Figure 2.6 shows a 1D slice from the generated 3D Vp model. Velocity increases indicate identifiable key target layers, including the base of significant ice bearing permafrost, base of ice bearing permafrost, the D1 hydrate sand unit, and

the B1 hydrate sand unit. I used a 60 Hz Ricker wavelet to forward model synthetic shot gather data and then applied the same wavelet when forward modeling the source wavefield during the RTM procedure.
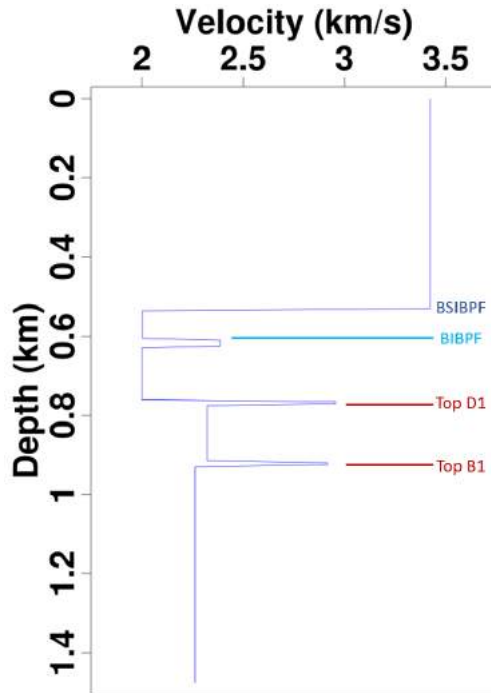
Figure 2.6 1-D slice from the 3-D Vp model generated in Petrel. Vp velocity values range from 2.0 km/s to 3.4 km/s. Key targets can be identified including the base of significant ice bearing permafrost, base of ice bearing permafrost, the D1 hydrate sand unit, and the B1 hydrate sand unit.

Figure 2.7 shows the results of the synthetic data test using a zero-lag correlation imaging condition. I have labeled the four key reflectors on the image: the base of significant ice bearing permafrost, the base of ice bearing permafrost, the top of D1 hydrate reservoir, and the top of B1 hydrate reservoir.
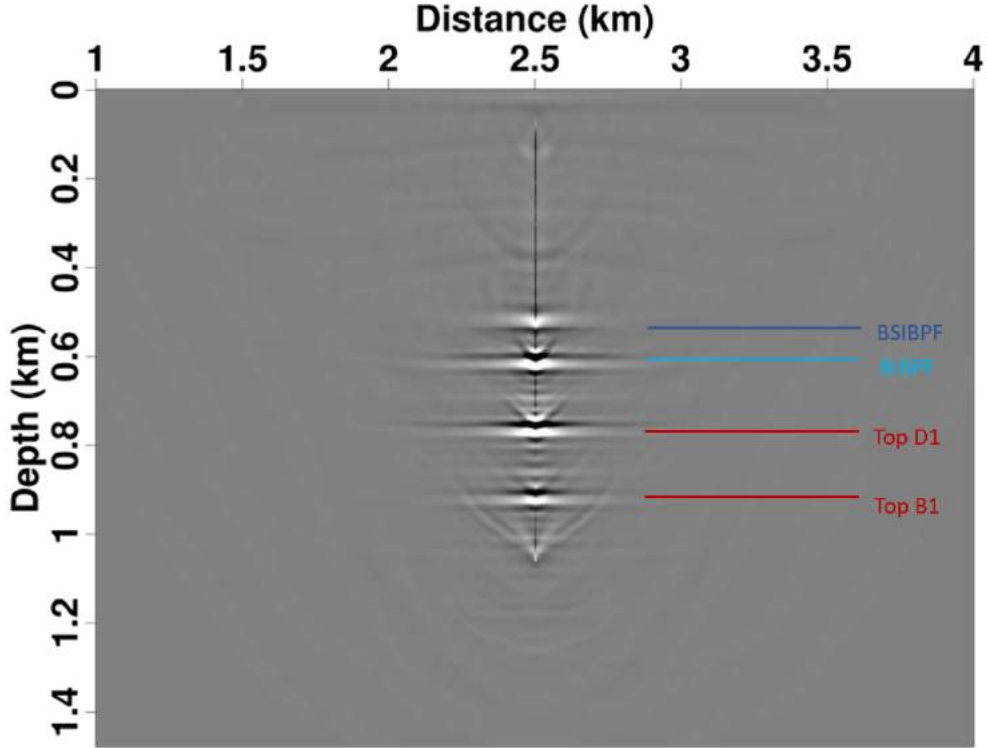
Figure 2.7 2-D acoustic RTM result using a standard zero-lag correlation imaging condition.

2.2.4   3D RTM Code Development and Validation

After using the 2-D velocity model and synthetic data to validate the 2-D RTM code and imaging process, I subsequently expanded the existing RTM code into a 3-D version. Initial testing and development were done with the full 3-D synthetic velocity model. Following the expansion into a 3-D version, DAS 3-D VSP field data was ready to be used over synthetic data. Key contributions were made by other project team members to assist with data preprocessing and velocity model development (see Author statement in Appendix B). These steps included processing the DAS VSP strain-rate data to isolate the P-wave reflections and extract a 1-D velocity model from the shot gathers. After extracting the 1-D extracted velocity model into a 3-D model, the team applied a 3-D tomographic velocity model building analysis to computing additive Vp model perturbations. Chapter 3 and covers these processing steps in greater detail.

The high-quality and high-frequency data associated with this DAS 3-D VSP data set motivated applying 3-D RTM imaging on a fine grid with $\Delta x = \Delta y = \Delta z = 3.0$ m discretization intervals and a 2.544 $\times$ 2.544 $\times$ 1.920 km^3 model size, which resulted in a large 3-D model domain of $N_z \times N_x \times N_y = 640 \times 848 \times 848$ grid points. We interpolated the Vp model output from the 3-D velocity refinement to a uniform 3.0 m grid, which was input with the processed data to the 3-D RTM engine.

The final step in the RTM process involves the application of an imaging condition to combine the propagated source and receiver wavefield information to construct a single 3-D image volume. Here, I stack together 90 single-shot images into a single global image volume. Figure 2.8a presents a 2D slice south of the wellhead location constructed using zero-lag correlation imaging conditions. Figure 2.8b shows the equivalent result using a energy normalized imaging condition using $\epsilon = 10^{-5}$ to prevent zero division. The energy normalized imaging condition has imaged extended lateral reflectivity, which leads to improved reflector illumination throughout the volume. Additionally, the observed reflectors are higher resolution and with improved amplitude balance. However, applying the energy normalized imaging condition also has increased imaging artifacts that need to be addressed by applying post-migration noise-suppression techniques.
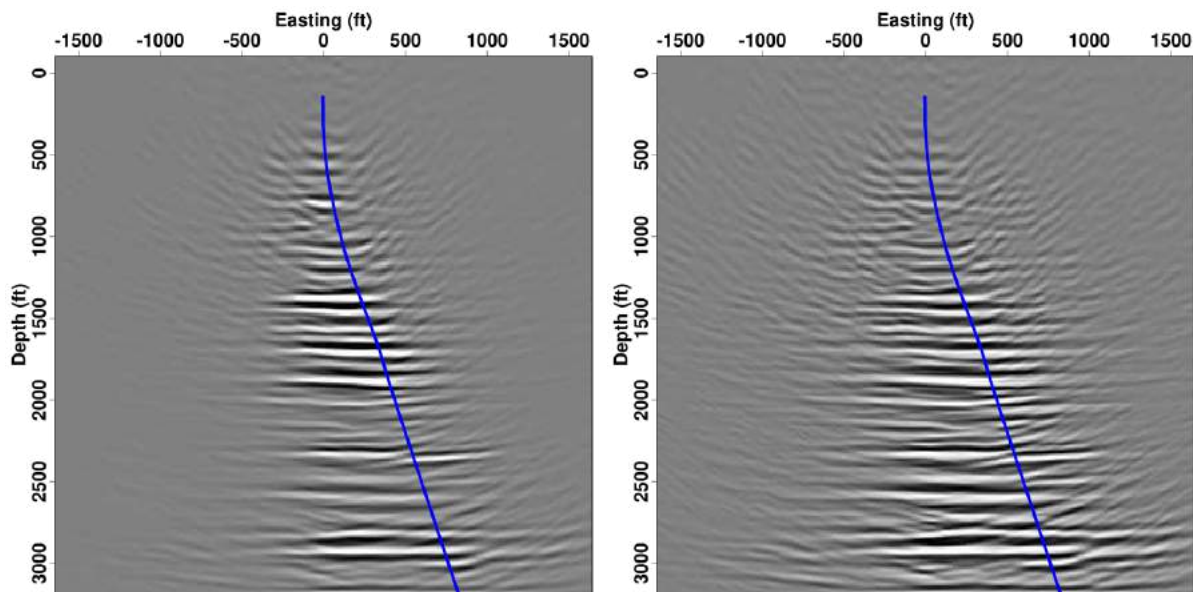
Figure 2.8 2D slice extracted from a 3D acoustic RTM image formed by stacking 90 individual shot images consructed using (a) zero-lag correlation and (b) energy normalized imaging conditions.

2.3   Post-Migration Noise Suppression

Applying the 3-D RTM process clearly generates interpretable images that represent subsurface reflectivity; however, high-angle migration swing artifacts also clearly contaminate the image volume. Post-migration noise suppression can remove non-geologic features as well as increase reflector illumination. This can be done by applying a mute or through a dip-filtering process that removes a substantial amount of noise within the image [23]. Drawbacks to applying noise suppression are the potential for removing true geologic features that may appear to be noise (e.g., dipping faults). Thus, these processes must be used

judiciously.

After running a number of tests, I selected dip filtering as the primary noise suppression method to be applied to the stacked 3-D RTM image volume. The main purpose of applying this filter was to remove the steeply dipping artifact noise (i.e., migration swings) appearing within the permafrost region and throughout the lower model sections. Dip-velocity filtering is a transform-mute-inverse transform method that uses the velocity model and reflector dips to compute a mute window to remove the steeply dipping artifacts thought to be of non-geologic origin. After computing the global image volume, I applied velocity-dip filtering to remove suspected artifacts. Figure 2.9 shows the energy normalized imaging condition with the velocity-dip-filtering process applied. The velocity-dip-filtering process is able to maintain the resolution and amplitude of the reflectors throughout the model, while successfully removing the previously visible steeply dipping migration artifacts.
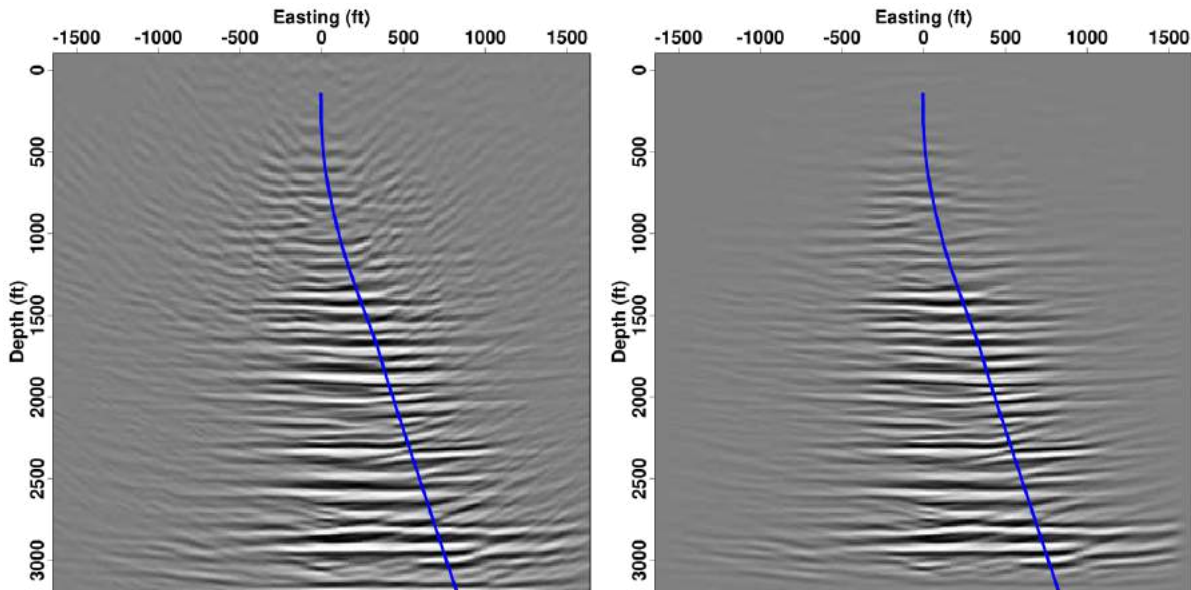
Figure 2.9 2-D slice extracted from the 3D acoustic RTM energy normalized image volume (a) before and (b) after applying the velocity-dip-filtering process.

2.4 Summary of Addressed 3-D RTM Challenges

Applying RTM is a straightforward process using the 3-D FDTD solver to calculate wavefield propagation; however, during this process several field-data-specific imaging challenges arose during the imaging process that needed to be addressed in the RTM code and imaging process: high-frequency data content, handling irregular data and model geometry, and borehole deviation.

2.4.1 DAS VSP Frequency Content

Using conventional surface geophone recording methods, the recorded data are of a lower-frequency content due to two-way wavefield propagation. However, with VSP recording methods recorded data are higher frequency due to the largely one-way travel paths from source to receiver. Moreover, DAS fiber acquisition allows for even higher frequency data from the dense receiver measurements along the length of the well. Typically, RTM methods use a source wavelet with a 50-60 Hz maximum frequency [24] because model size and sampling restrictions lead to significant computational requirements. Thus, typical RTM analyses do not take full advantage of the frequency content contained within DAS 3-D VSP data.

To use the full frequency spectra of the dataset, herein I used a finely spaced velocity model and small wavefield propagation steps frame, which enabled the use of a 100 Hz maximum Ormsby wavelet higher-frequency wavelet and a high-frequency RTM procedure to be carried out. This led to improved high-resolution of target reflectors and promoted a better understanding of the local geology and subsurface structure.

2.4.2 Irregular Surface Geometry

Irregular data acquisition in active seismic surveys can be challenging for computational modeling when source (and receiver) locations do not align with the model grid locations. This poses a modeling challenge because spatially accurate data injection is important for the wavefield reconstruction and propagation processes, and inaccurate handling of measurement locations not on grid points may lead to inaccurate data results.

In this field data set the measurement datum of acquisition site was slightly variable from 11 m to 17 m above sea level, and the source locations were in a radial pattern surrounding the well head. To handle the variability of the surface points on a grid size of 3.0 m and the values changing no more than 6.0 m, I used an inverse-distance weighting scheme to approximately account for the noted elevation changes. This split the elevation value into multiple grid points to accurately account for the true elevation. The same technique was used to handle the lateral spatial location of the source locations due to the radial shot pattern and not perfectly aligned with the Cartesian grid.

2.4.3 Borehole Deviation

VSP surveys by nature often exhibit borehole deviations; thus, the RTM process must account for the irregular receivers downhole during wavefield propagation. Similar to the irregular surface geometry, this is a challenge for data injection and wavefield propagation because the receivers typically do not fall directly on grid points. I used the same inverse-distance weighting technique to scale the data injection at different

model locations to account for the true data locations, which allowed the 3-D spatial location of the well trajectory to be accurately accounted for during the wavefield propagation and data injection procedures.

CHAPTER 3

ADVANCED DISTRIBUTED ACOUSTIC SENSING VERTICAL SEISMIC PROFILE IMAGING OF AN ALASKA NORTH SLOPE GAS HYDRATE FIELD

Cullen Young[2,3,4], Jeffrey Shragge[5], Whitney Schultz[5,6], Can Oren[5], Seth Haines[7], Jim Simmons[5] and Tim Collett[7]

3.1 Abstract

Gas hydrates are found in significant quantities on the North Slope of Alaska in sub-permafrost sand units and intermixed in lower portions of permafrost within the hydrate stability window. While conventional surface seismic data and established imaging methods can indicate the presence of gas hydrate reservoirs, producing high-resolution images of (seismically) thin layers remains challenging due to the preferential attenuation of the higher-frequency data components. An alternative strategy is to use distributed acoustic sensing (DAS) involving cementing optical fibers into boreholes to measure seismic wavefield energy closer to the strata of interest using vertical seismic profiling (VSP). DAS VSP imaging takes advantage of the shorter travel paths and reduced attenuation to generate higher-resolution near-well images. We illustrate these benefits on a DAS VSP data set acquired at the Hydrate-01 stratigraphic test well located in the Prudhoe Bay Unit of Alaska where significant gas hydrate deposits have been detected in two sub-permafrost sand layers that are intended for long-duration production testing. Our DAS data preprocessing workflow effectively isolates the upgoing compressional-wave (P-wave) reflections required for subsurface acoustic imaging. After applying three-dimensional (3-D) tomography to improve the quality of the 3-D migration velocity model, we use 3-D reverse-time migration (RTM) to develop high-quality images of the two target sands and minor near-well faulting. We validate our RTM images through highly accurate well-ties with previously acquired petrophysical log data. This study demonstrates that combining 3-D RTM imaging with DAS VSP data provides significant value to gas hydrate and similar projects, and it suggests that more advanced inversion approaches such as (elastic) least-squares RTM could recover higher-resolution and more quantitative estimates of subsurface reflectivity, which would be valuable for

---

[2]Primary researcher and author.
[3]Author for correspondence
[4]Graduate student, Colorado School of Mines, Golden, Colorado, USA.
[5]Colorado School of Mines, CO, USA.
[6]Occidental Petroleum, Houston, TX, USA.
[7]United States Geological Survey, Denver, CO, USA.

refining the understanding of gas-hydrate systems.

3.2 Introduction

Developing a better understanding of subsurface gas hydrate deposits is an important scientific objective because of their potential as not only an energy resource [25] but also as a contributor to global climate change [26]. Gas hydrates are found in Arctic permafrost regions within a narrow gas hydrate stability zone, and in in some areas high-porosity sand units exist with sufficient thickness to host larger accumulations that offer potential for commercially viable extraction. Hydrate-bearing units are often clearly distinguishable in petrophysical log data as well as in drill core samples. Establishing the presence of these units at locations away from boreholes, though, generally requires further geophysical analysis and, in particular, three-dimensional (3-D) seismic imaging work that is capable of resolving the often thin (tens of meters) stratigraphic layers.

Surface 3-D seismic acquisition has long been an important geophysical technique for developing subsurface constraints away from wells [27]. However, acquiring high-quality surface seismic data in Arctic permafrost regions is often quite challenging due to the presence of complex near-surface velocity variations, the often significant wavefield attenuation, the limited seasonal acquisition window, and other logistical considerations[28]. Thus, alternate and complementary seismic imaging methods are increasingly being used that help address or circumvent these issues.

Over the past decade, distributed acoustic sensing (DAS) has emerged as an important technology for seismic investigation [7]. A DAS sensing system in a borehole application is composed of two key components: (1) a deployed optical fiber cable that is usually elastically coupled to the borehole during the cementing completion process; and (2) an interrogator unit (IU) that sends short laser pulses along the fiber and detects the light energy backscattered from minor heterogeneities within the fiber. When optical fibers are completely stationary, the IU measures no temporal phase shift within the detected backscattered signal; however, when a fiber is strained, for example by a passing seismic wave, the very small deformations associated with the wave disturbance lead to phase shifts in the backscattered signal that the IU measures as a seismic-data-like quantity (usually in strain-rate format). DAS observations measured along the fiber usually are very dense [e.g., at 3.0 ft (1.0 m) intervals] [5], which allows for high-quality seismic wavefield measurements that usually would be prohibitively expensive for the corresponding geophone installations [6]. However, DAS systems are not a panacea for subsurface seismic detection because the fiber systems are only sensitive to along-fiber axis strain components, meaning that some waveforms are not measurable, in addition to areal extent and surface access limitations [29].

DAS seismic acquisition in boreholes using vertical seismic profiling (VSP) is becoming increasingly common in the oil and gas industry [4] because of the relatively low cost of installing optical fiber in boreholes, which can remain in place for the lifetime of a project and greatly contribute to 3-D and repeat (i.e., time-lapse) VSP surveying activities. Applying advanced 3-D seismic migration algorithms then can lead to high-resolution seismic imagery that assists with developing a better understanding of the 3-D geological structure controlling gas-hydrate systems. In addition, it can be used for time-lapse surveying the dynamic responses from, and the underlying rock physics of, hydrate production.

This paper investigates the utility of DAS 3-D VSP surveying for DAS installation at the Hydrate-01 stratigraphic test well (STW) drilled in the Prudhoe Bay Unit on the North Slope of Alaska as part of a collaboration among the U.S. Department of Energy (DOE) National Energy Technology Laboratory (NETL), Japan Oil, Gas and Metals National Corporation (JOGMEC), and the U.S. Geological Survey (USGS). The Hydrate-01 well [30] and other local and regional wells have confirmed the presence of regionally extensive gas-hydrate reservoir intervals beneath the approximately 2000 ft (600 m) thick local permafrost layer. The two 40 ft (12 m) thick sand layers (D1 sand within regional unit D and B1 sand within unit B) [31] hosting the gas hydrates deposits are interpretable from a regional 3-D surface seismic survey [32]; however, additional high-resolution details about the gas-hydrate system and minor near-borehole faulting are sought by the project team. To support the gas-hydrate production project efforts, a large-scale DAS 3-D VSP data set was acquired in winter 2019, with the goal of providing additional insight about these issues.

Herein, we report our work in developing and applying a data processing sequence, refining a 3-D velocity model, and implementing an advanced seismic prestack depth migration (PSDM) that produces high-quality and accurately well-tied images that support broader project objectives. The paper begins with a geological overview of the Alaska North Slope project area and highlights the petrophysical data associated with the Hydrate-01 STW. We then discuss the acquisition of the DAS 3-D VSP data set and illustrate the high-quality measurements afforded by DAS technology. Next, we detail our seismic preprocessing workflow and time-imaging efforts using one-dimensional (1-D) velocity models. After highlighting observations showing the departure of seismic data from an approximately 1-D earth, we discuss our approach for the development and refinement of a 3-D P-wave velocity model required for high-resolution reverse-time migration (RTM) imaging analysis. After detailing our RTM implementation, we present high-frequency (100 Hz) 3-D VSP RTM imaging results that clearly show the target gas hydrate bearing sands as well as minor near-well faulting. We also present accurate well-tie comparisons to help validate the VSP RTM imaging procedure. The paper concludes with a discussion about more advanced inversion approaches, including least-squares RTM (LSRTM), which could be applied to further improve

image resolution as well as provide more quantitative estimates and informed interpretations of the observed subsurface reflectivity associated with the gas hydrate deposits.

3.3   Geologic Overview

The gas hydrate field site area is located at the Kuparuk 7-11-12 well pad within the Prudhoe Bay Unit of the North Slope of Alaska (see Figure 3.1). The geology in this region has been investigated previously through surface 3-D seismic acquisition and various targeted drilling programs [33]. A long-standing and extensive geological, petrophysical, and geophysical characterization effort [34] based on these data has confirmed the regional presence of gas hydrate-bearing reservoir units of significant volume within the gas hydrate stability zone.

The geological sequences most pertinent to the present investigation are found in the regional Eileen gas hydrate trend [31], which contains gas hydrates typically observed below ice-bearing permafrost [35]. The associated hydrate-bearing intervals occur within the largely transitional marine to non-marine, sand-rich, Sagavanirktok Formation with the highest quality reservoir units being characteristically very well sorted fine-grained sands to coarse silts [36]. The Eileen trend has an approximate 2°–3° eastward dip and is dominated by a series of normal faults with roughly north-south orientation [35]. The laterally extensive and variable sand reservoirs along with overlying sealing layers and normal faults provide conditions that allowed for complex stratigraphic-structural entrapment of hydrocarbon resources [35]. These geological observations and overall logistical and cost advantages make the Prudhoe Bay Unit a unique location for developing a long-term and large-scale hydrate production test facility.

In December 2018, the Hydrate-01 STW was drilled at the Prudhoe Bay Unit site to a total depth of 3289 ft (1002 m) [30, 37]. Note that all depth values are quoted in true vertical depth (TVD) subsea using the mean sea level as a reference datum (the well pad is 56.2 ft above mean sea level). Based on existing 3-D seismic data (not available to the authors) and previous regional boreholes, a key goal was to intersect two inferred hydrate-bearing sand layers (referred to herein as the D1 and B1 sands) that exist within regionally extensive D and B stratigraphic units. The drilled borehole remained vertical until 300 ft (91 m) where it began to deviate at roughly 15° from vertical at an azimuth of 65.5° from true north with 959 ft (292 m) of total offset from the wellhead location at total depth [30]. During the drilling operation a suite of logging while drilling (LWD) petrophysical logs were acquired to identify the key lithological units and confirm the presence of significant hydrate-bearing zones. During well completion, two multimode optical fiber cables (distributed temperature sensor - DTS and distributed acoustic system - DAS sensors) were installed along the borehole for use in future geophysical monitoring programs. The STW confirmed high gas hydrate saturations in the target layers, establishing Kuparuk 7-11-12 to be suitable for further

reservoir testing [30, 32].

Figure 3.2 presents petrophysical logs acquired during the Hydrate-01 LWD program [37]. The first track shows three overlain logs: caliper (green curve), bit size (black line) and gamma ray (GR; filled in scale). The caliper log shows variation beyond the nominal 9 5/8" hole diameter from near the surface through 2057 ft (627 m) depth; however, less variation is noted below this depth level to total depth through the 5 1/2" bore. Tracks 3–5 respectively show the resistivity, density, and together the P- and S-wave sonic logs. Names for the key identified stratigraphic units are located to the right of the plots. We note that the logs in tracks 3–5 down to 1600 ft (488 m) (i.e., at the C17 marker) similarly show significantly higher variation than at greater depths. While the significant decrease in sonic velocities at 1600 ft (427 m) may suggest that this depth represents the base of significant ice-bearing permafrost (BSIBPF), temperature logs suggest that the interpreted base of ice-bearing permafrost (BIBPF) is at 1883 ft (574 m).

Figure 3.3 presents an enlarged view of the petrophysical logs within the depth interval of interest. While there are at least five regionally extensive layers (units E–A) within which hydrates have been identified within the greater Prudhoe Bay Unit area, only two contain gas hydrates at this site. Based on the petrophysical log data, the top of the shallower D1 sand is located within regional unit D at 2294 ft (699 m), with a thickness of 37 ft (11 m), and is at a temperature of roughly 4.2°C. The top of the deeper B1 sand is within unit B at 2769 ft (844 m), with a thickness of 43 ft (13 m) and a temperature of roughly 12.2°C. These two sands fall within the hydrate stability zone and represent the main targets of the seismic imaging work reported in this paper. The STW also intersected a minor fault with approximately 15 ft (4.5 m) of displacement at the D1 sand, which introduces a minimal technical risk to any potential hydrate production test and thus represents a secondary target of the seismic imaging program.

3.4   DAS 3-D VSP Data Set

Active-source seismic data are commonly acquired using a Vibroseis seismic energy source that vibrates the ground in a multi-second "sweep" from low to high frequencies. This action generates wave energy that propagates into the subsurface, interacts with discontinuous earth structure (i.e., seismic "reflectors"), and generates scattered energy that propagates upward to the surface where the arriving waveforms are recorded by sensitive receivers (i.e., geophones). Land seismic surveying generates a variety of P-, S- and surface-wave energy; however, standard approaches, like the acoustic imaging analyses presented herein, use only P-waves with the other arrivals representing "noise" that need to be removed through a data preprocessing effort. Another challenge is that higher-frequency wavefield components preferentially attenuate relative to lower frequencies during subsurface propagation due to anelastic behavior. As a

result, the frequency content of reflected P-wave signals recovered at the surface often is too low to resolve the thin [e.g., $40 - 50$ ft ($12 - 15$ m) or less] lithological layers of interest.
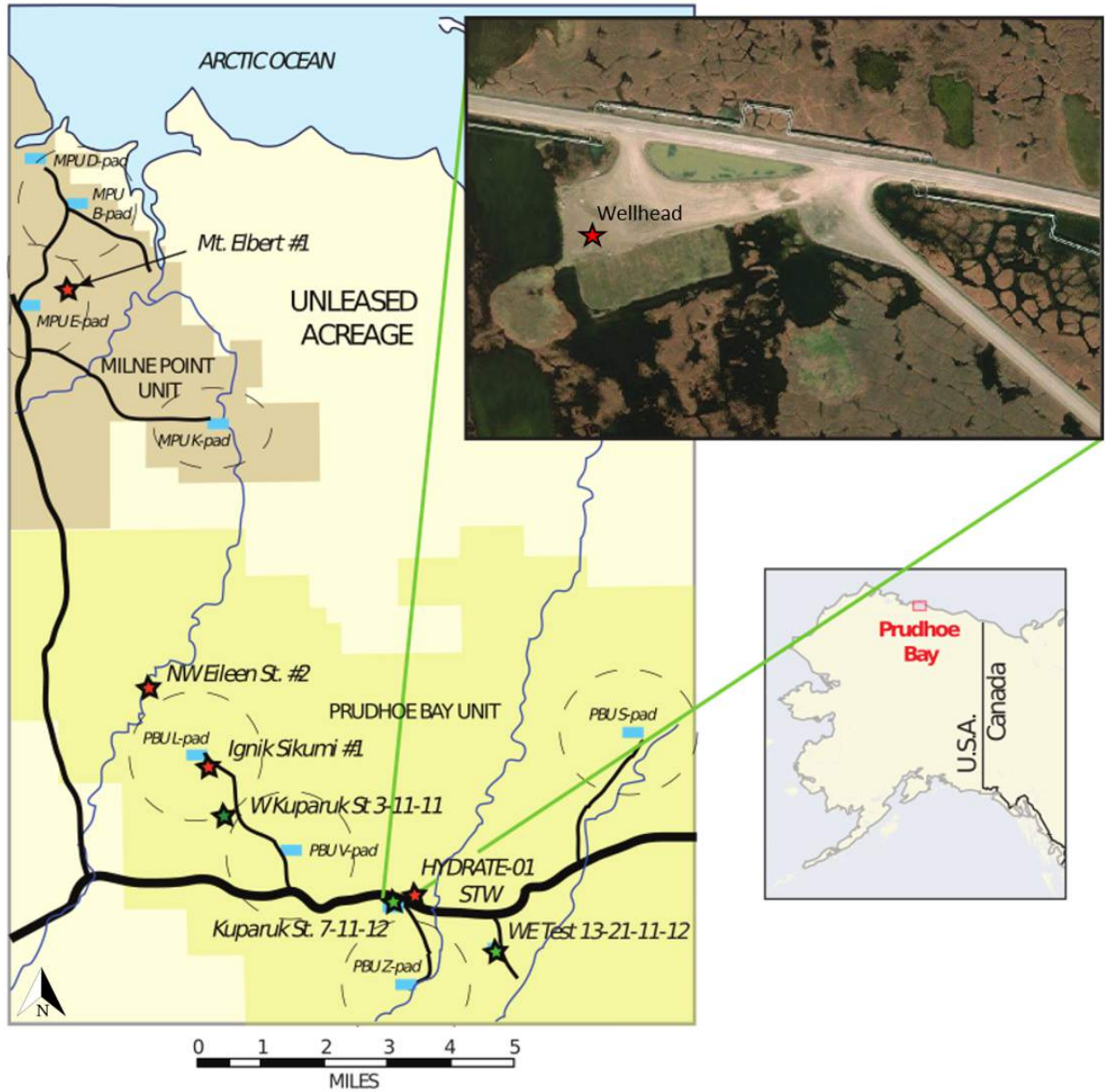
Figure 3.1 Location of the Hydrate-01 stratigraphic well (HYDRATE-01 STW) gas hydrate research site in the Prudhoe Bay Unit with other regional test wells. The photograph to the upper right of the image shows the well pad area. The lower right inset shows the location of the project with respect to the state of Alaska. Modified from Boswell et al. (2022).
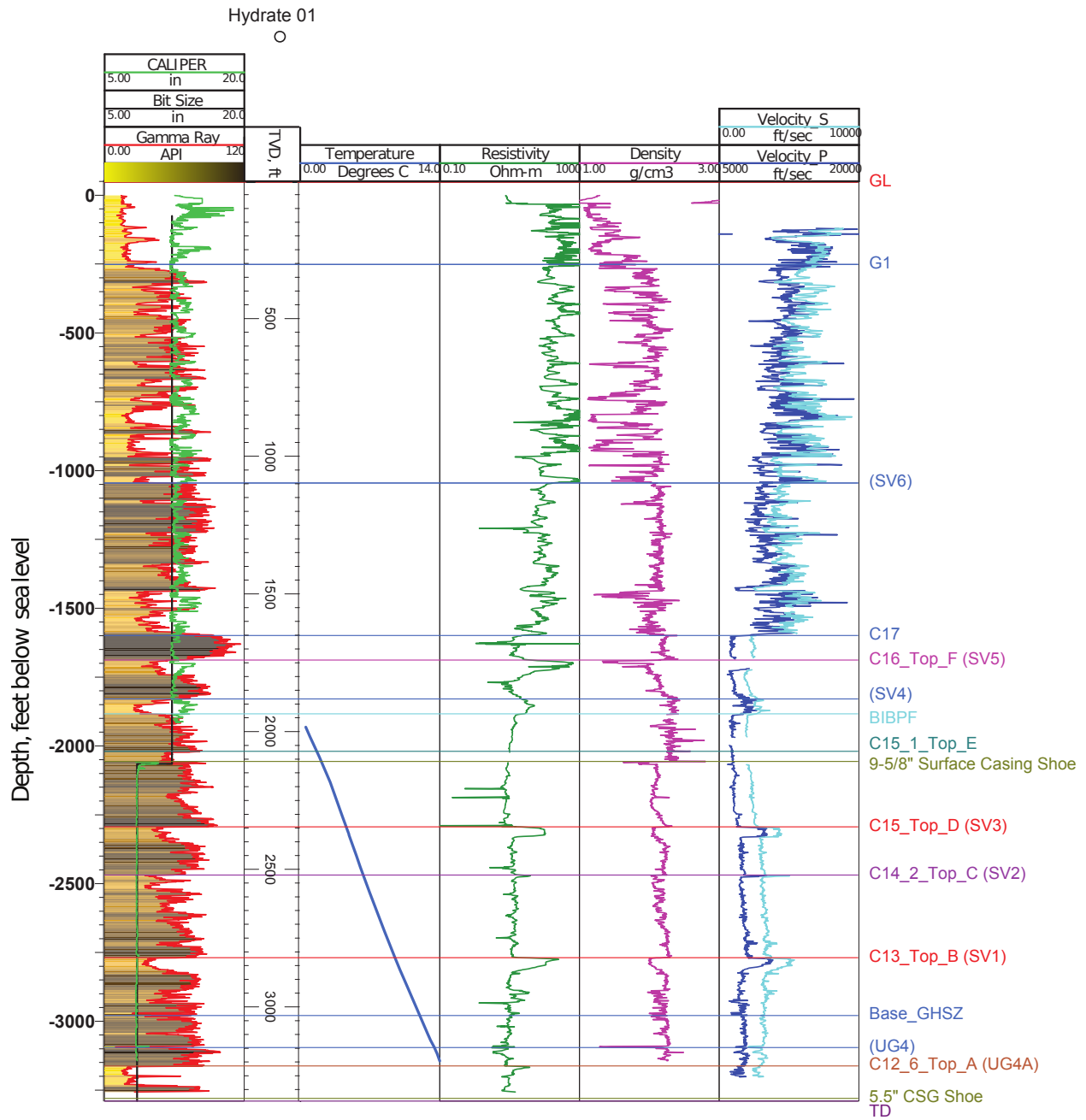
Figure 3.2 Key petrophysical logs acquired at the HYDRATE STW-01 well. Tracks (from left to right): (1) Caliper (green), bit size (black) and gamma ray; (2) inferred temperature; (3) resistivity; (4) density; and (5) S- (cyan) and P-wave (blue) sonic velocity. Key stratigraphic units are indicated to the right of the figure. C15_Top_D (SV3) and C13_Top_B (SV1) indicate the tops of units D and B. Our target reservoirs, referred to the D1 and B1 sands, are located at the tops of units D and B. The interpreted base of significant ice-bearing permafrost (BIBPF) is located at 1883 ft (574 m). Data are presented with further description by Collett et al. (2022).
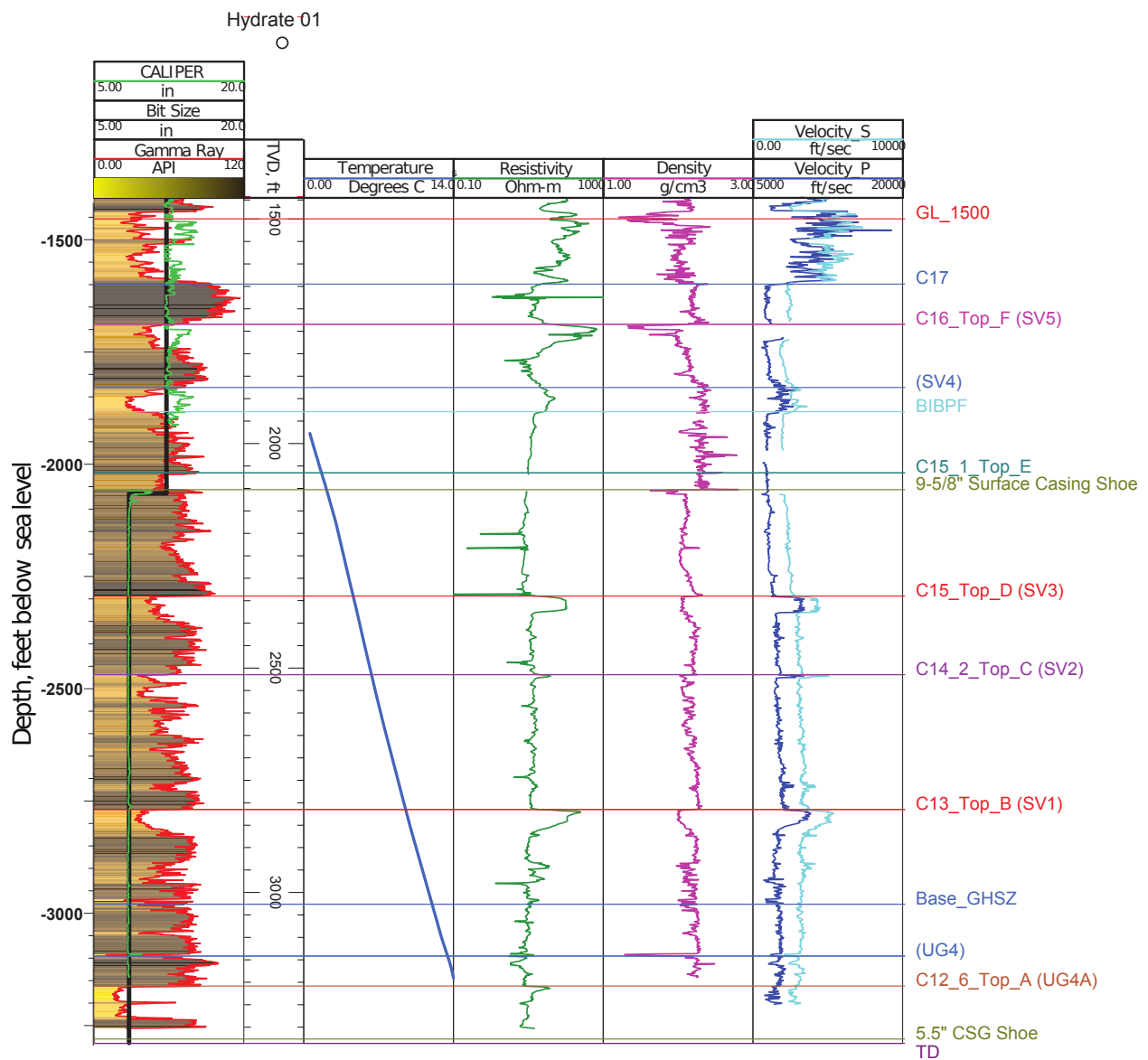
Figure 3.3 Enlarged view of the well logs presented in Figure 3.2 below 1500 ft true vertical depth (TVD). The tracks are plotted in the same configuration. The D1 and B1 sands are clearly visible in the presented log data as a significant reduction in gamma ray (trace 1) and density (trace 4) and increase in resistivity (trace 3) and P- and S-wave velocities (trace 5). No temperature effect is observed on Trace 2. Data are presented with further description by Collett et al. (2022).

To address these issues, seismic surveying can be conducted with receivers located in a borehole rather than at the surface, a geometry referred to as a vertical seismic profile (VSP). Two advantages of this approach are that: (1) VSP data are often largely free of noisy surface-wave energy leading to more straightforward data preprocessing and clearer seismic images; and (2) wavefields are measured without having to propagate back up to the surface, which reduces the overall travel-path lengths and helps

minimize attenuation-related effects, including those due to highly heterogeneous near-surface materials. Together these advantages can result in higher-frequency seismic data and higher-resolution images.

While 3-D VSP surveys have been used in industry for more than half a century, the overall impact of 3-D VSPs surveys has been fairly limited due to the challenge of instrumenting a borehole with a sufficient number of seismic sensors. However, the recent decade has seen the development of DAS technology that can turn optical fiber into a distributed sensing network capable of acquiring dense measurements (e.g., every meter) along the entire deployed fiber length. In general, DAS data acquisition measures the component of ground motion that strains the fiber along the deployment axis and is well situated to measure strains introduced by the near-vertically incident downgoing body waves. Accordingly, DAS surveys are increasingly being used in 3-D VSP seismic monitoring scenarios due to: (1) the relatively low cost of procuring optical fiber that is permanently cemented into wells during borehole completion, and (2) the resulting DAS fiber installation enabling long-term monitoring over the lifetime of the project. It is important to note that while DAS 3-D VSP surveys can provide high-resolution seismic images, the acquisition geometry and the DAS fiber array sensitivity constrain the imaging aperture to a limited area around the borehole.

A DAS fiber optic cable system was cemented to the well casing in the STW [38], which allowed for seismic wavefields to be measured every 3.0 ft (0.9 m) from a depth of 48 ft (15 m) to 3506 ft (1069 m) TVD below the target hydrate layers (994 sensing depths in total). The DAS VSP data were acquired with a Silixa DAS acquisition system using a 10-foot (3 m) gauge length, meaning that seismic traces are obtained for each 3-m section of cable, which was chosen to optimize signal-to-noise (S/N) levels of the recorded data.

DAS 3-D VSP data were acquired using a vertical Vibroseis source running a 20.0 s sweep between 2 and 200 Hz [39]. Figure 3.4 shows the 1701 Vibroseis source locations acquired in a dense radial pattern surrounding the well head (herein taken to be the relative coordinate system origin) that largely avoided pre-existing landscape and infrastructure features such as roads, lakes, and pingos. The maximum source-wellhead offset of 3517 ft (1072 m) allows for a reasonable imaging aperture for undertaking full-wavefield seismic migration experiments. The DAS data were acquired in a strain-rate format as 4.0 s shot records at a temporal sampling of 0.1 ms. Prior to delivery from the contractor, the Vibroseis data were correlated, had multiple sweeps at the same point stacked to form a single shot gather per source point, and converted to particle displacement format.

The left column of Figure 3.5 presents three representative shot gathers acquired at near, mid, and far offsets, respectively, while the right column illustrates interpreted arrivals for the corresponding panels to the left. The near-offset gather data at 550 ft (168 m) (Figure 3.5a) show clear P-wave first arrivals

downhole (here, the horizontal axis) with a significant amount of upward-reflected energy that forms "V-like" patterns. Figure 3.5b shows the direct P-wave arrivals as a red curve and one of the reflected P-P events as a blue curve. The dashed green line indicates the interpreted BSIBPF, to the right of which the slopes of the marked arrivals steepen indicating significantly slower P-wave velocities.
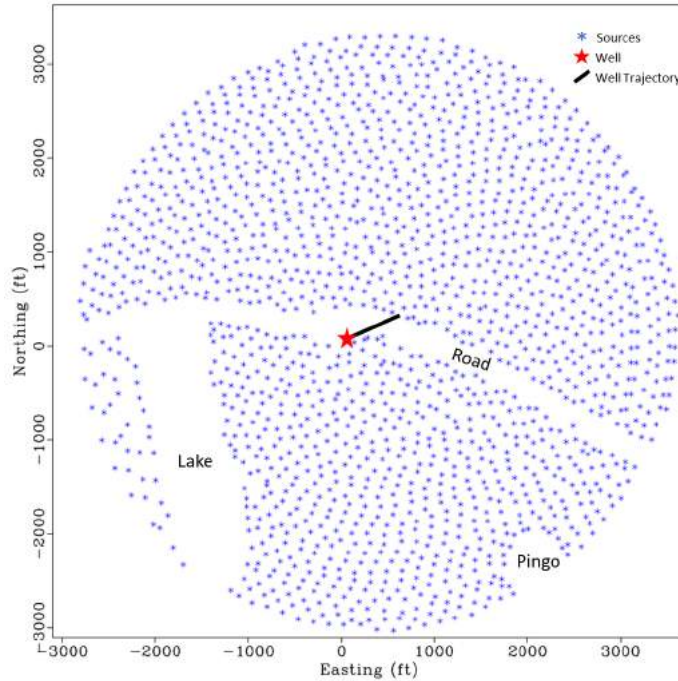
Figure 3.4 Distributed acoustic sensing (DAS) three-dimensional (3-D) vertical seismic profile (VSP) survey acquisition geometry. A total of 1701 source locations (blue dots) were acquired in a radial pattern to a maximum of 3517 ft offset about the well head (shown as a red star) located at origin of a relative coordinate system. The black line shows the well deviation oriented 65.5° from north to a maximum of 959 ft. Data are presented with further description by Tamaki et al. (2022).

Figure 3.5c and Figure 3.5d present a mid-offset gather at 1900 ft (579 m) that has higher-amplitude direct S-wave arrivals as well as upward-reflected S-S waves relative to the near-offset panels. Finally, Figure 3.5e and Figure 3.5f present a far-offset shot gather from 3500 ft (1067 m) with even stronger S-wave arrivals at depths below the interpreted BSIBPF. We note that the increase in S-wave energy at father offsets is likely due to the combination of both source radiation pattern as well as a more favorable angle-dependent sensitivity of the DAS recording system. We have also marked an example of a converted P-S wave that is interpreted to occur at the base of major ice. Overall, the DAS 3-D VSP data are very high quality, largely noise-free, and clearly exhibit a full range of expected elastic full-wavefield behavior. However, because this investigation focused on acoustic (P-wave) imaging, additional seismic data preprocessing work was needed to optimize the data set for the PSDM activities discussed below.
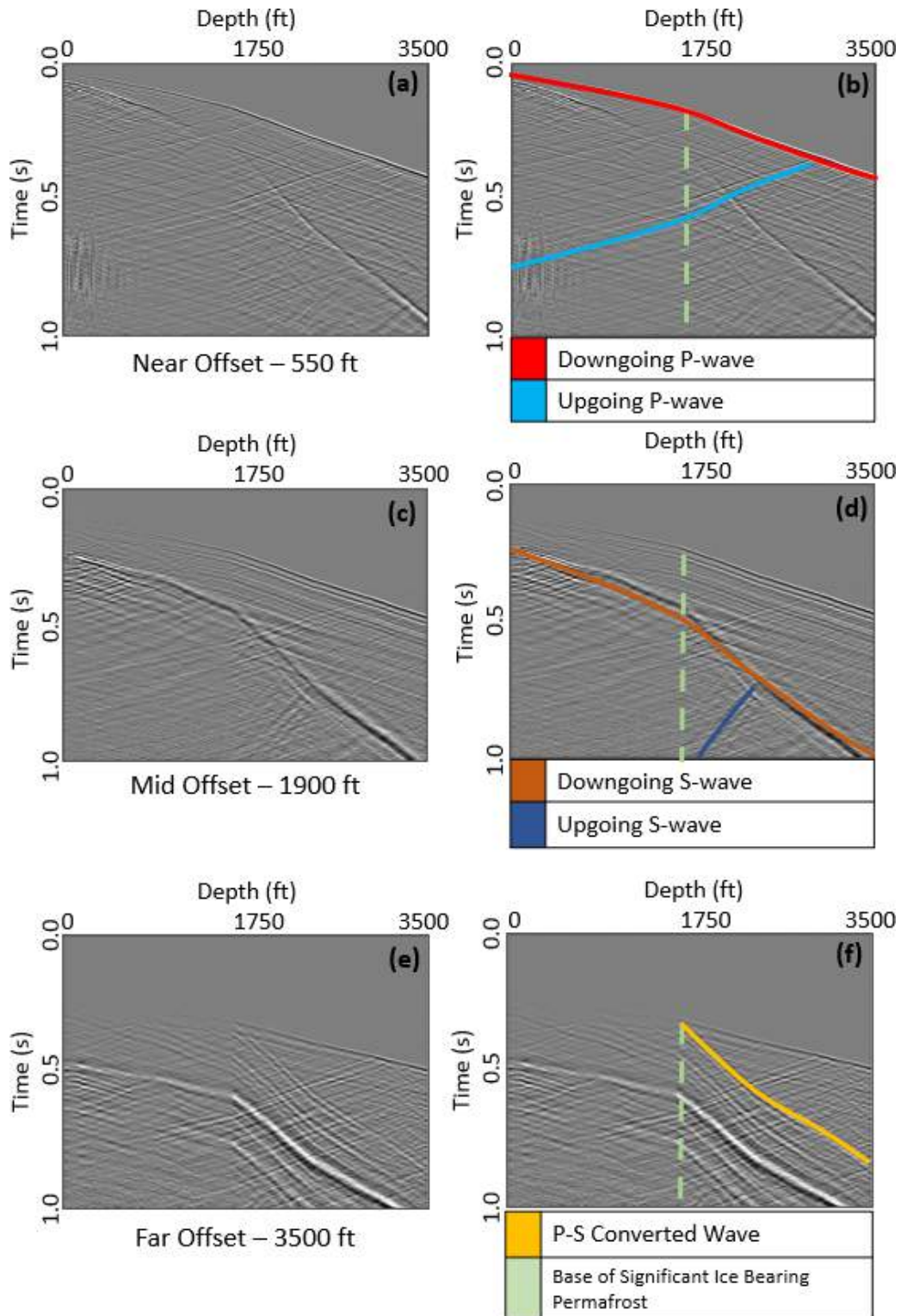
Figure 3.5 (a) Near-offset shot gather at 550 ft with (b) highlighting the direct P-wave arrivals and an example of an upgoing P-P reflection. (c) Mid-offset shot gather at 1900 ft with (d) marked direct S-wave arrivals and an example of an upgoing converted S-S reflection. (e) Far-offset shot gather at 3500 ft with (f) an example of a downgoing P-S conversion. The dashed green line represents the interpreted base of significant ice-bearing permafrost.

3.5 Data Preprocessing and Initial Stack

Preparing a DAS 3-D VSP data set for acoustic seismic depth imaging and related analysis requires a preprocessing workflow that is aimed at improving the S/N levels of the reflected P-wave energy relative to other wave types and background noise. To complete these tasks, we processed the acquired seismic data volume using a combination of the Shearwater Reveal [40] and Landmark Solutions SeisSpace [41] industry seismic processing packages.
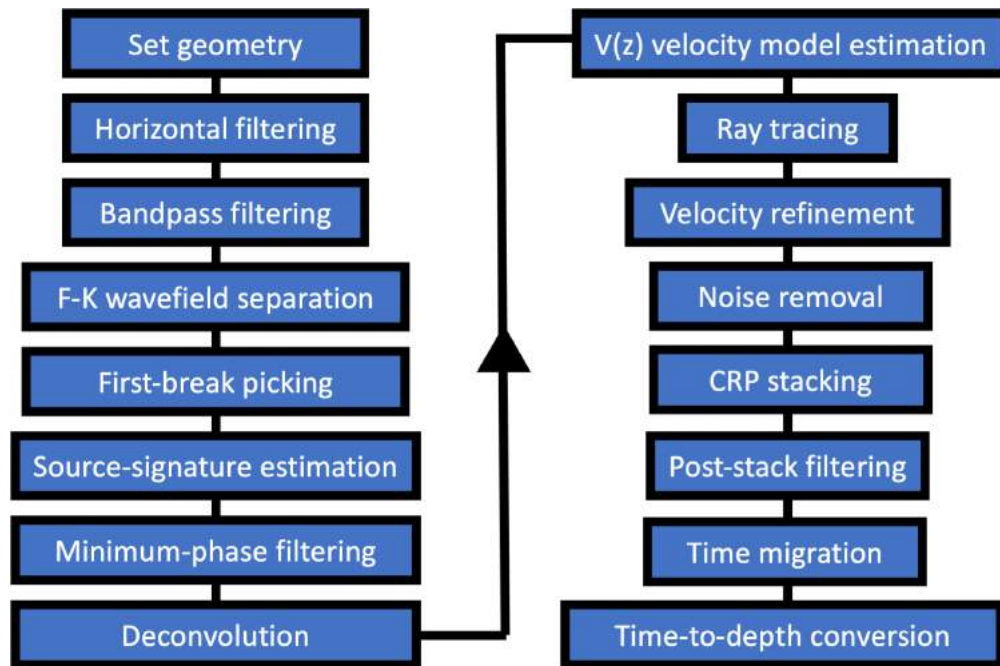
Figure 3.6 DAS 3-D VSP processing and time migration workflow.

Figure 3.6 presents our processing workflow from raw data import to the final time-migrated and depth-converted image volumes. The initial processing steps involved setting the acquisition geometry and applying a horizontal filter to attenuate minor linear DAS interrogator noise and a bandpass filter with 2-8-195-200 Hz corner frequencies to remove energy falling outside of the Vibroseis sweep band. Figure 3.7a presents a representative shot gather after this processing step that clearly shows P- and S-wave energy. These initial filtering steps led to minimal differences from the raw waveforms due to their already high data quality and S/N levels. Next, we applied up-down wavefield separation in the frequency-wavenumber domain to generate an upgoing data volume including both upgoing P- and S-waves. Figure 3.7b shows the effects of this processing step, where the resulting waveforms exhibit very little residual downgoing energy. We then estimated the source signature, filtered the data to minimum phase, and applied a deconvolution operator to remove the source signature and obtain flatter and more balanced spectra in the imaging band

of interest (Figure 3.7c). Finally, after transforming the data to the normal-moveout (NMO) domain (see below), we applied residual statics corrections derived from a custom ray-tracing tool and velocity refinement efforts, a residual filter to remove the contaminating S-wave reflected and P-S converted arrivals, and inverse NMO to recover a largely noise-free reflected P-wave data set (Figure 3.7d) appropriate for RTM.

3.5.1   1-D Velocity Model and NMO analysis

The next set of pre-imaging analyses involved developing a 1-D P-wave velocity model useful for S-wave filtering, $v(z)$ time migration [42], time-to-depth conversion, and generating a starting model for 3-D tomographic velocity refinement. Figure 3.8 presents several measured or derived velocity functions including the vertical-incidence VSP (VIVSP) estimate (pink), the processed P-wave sonic velocities (light blue), and three different smoothed approximations from the VIVSP data (red), and lightly (blue) and heavily (dark blue) smoothed sonic logs. The VIVSP and processed sonic velocity curves have similar structure, though the former tends to exhibit stronger shorter-wavelength variations. Both curves clearly show a significant velocity inversion around 1750 ft (533 m) measured depth, corresponding with the BSIBPF, below which the velocity profiles exhibit smaller variations and generally show increasing velocity with increasing depth. The imaging work reported below uses the heavily smoothed and decimated velocity function (dark blue), which likely underrepresents the P- (and S-) wave velocity gradients at the BSIBPF.

After developing a background 1-D $v(z)$ P-wave velocity model, the next steps involved performing ray tracing and NMO residual moveout analyses, which were completed separately to allow for additional quality control. The ray-tracing step calculated the traveltimes and reflection points for each source receiver pair, which are used to map the calculated (predicted) traveltimes of P-P VSP reflections to two-way vertical traveltimes. Ideally, the result of applying these statics corrections would be flattened or nearly flattened gathers that can be analyzed for velocity model accuracy and to see whether additional velocity analysis is required.

Figure 3.9 shows a compendium of shot gathers at six different source-well offsets that fall within six different azimuthal bins. This data sorting representation allows for a higher-level determination where the P-wave velocity model performs well by virtue of the flatness of the observed reflectivity; deviations from flatness within each gather provide insight into the robustness of the model for different offset-azimuth combinations. The overall reflector flatness on the gathers shown in Figure 3.9 suggests that the 1-D model performs fairly well; however, the noted small deviations, especially at farther offsets, indicate that the imaging processes would likely benefit from further 3-D velocity refinement, which is discussed in the following section.
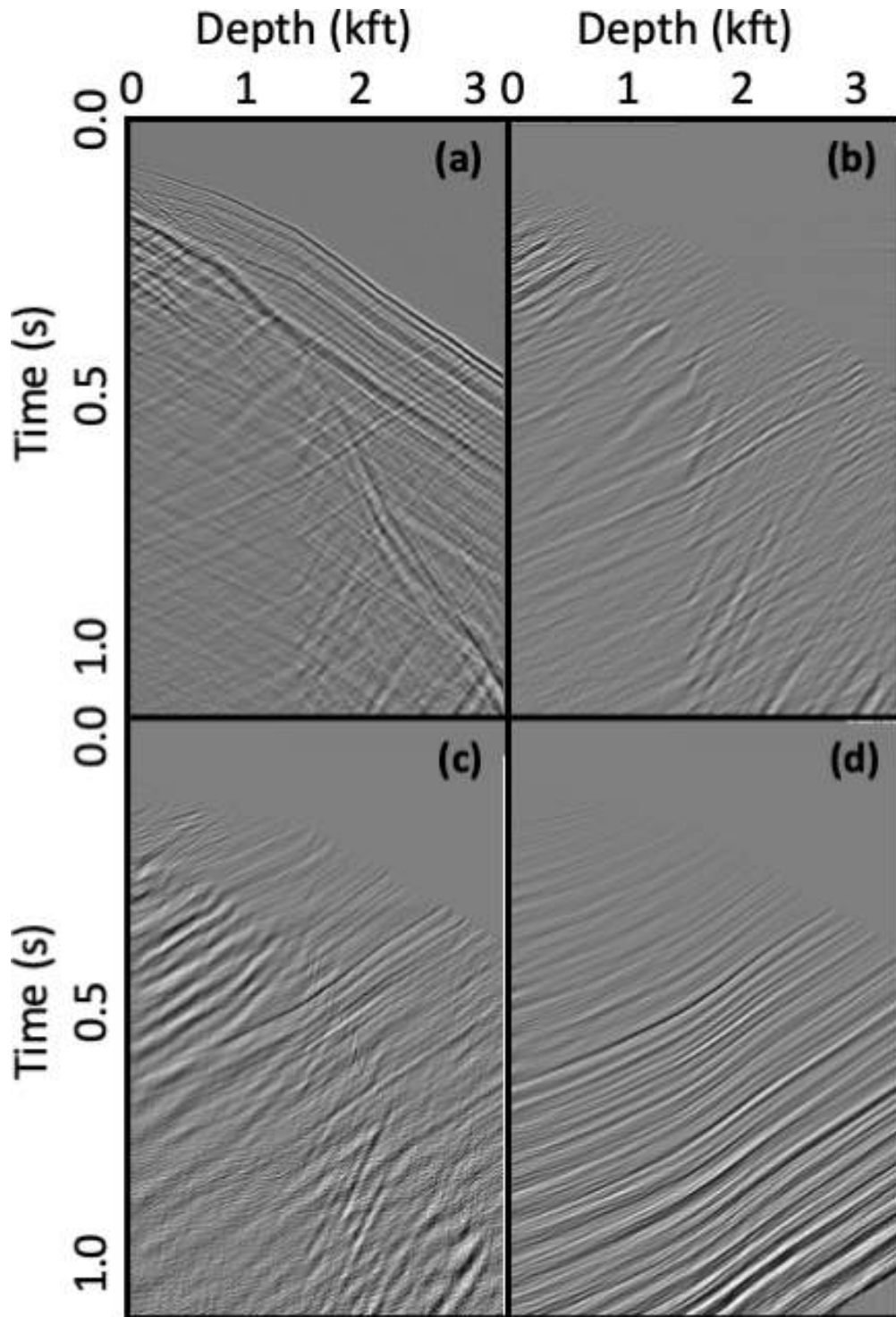
Figure 3.7 Illustration of key seismic data processing steps from Figure 3.6. Shot gather data after applying (a) horizontal and bandpass filtering, (b) $f - k$ up-down separation, (c) deconvolution, and (d) ray-traced reflection-traveltime corrections.
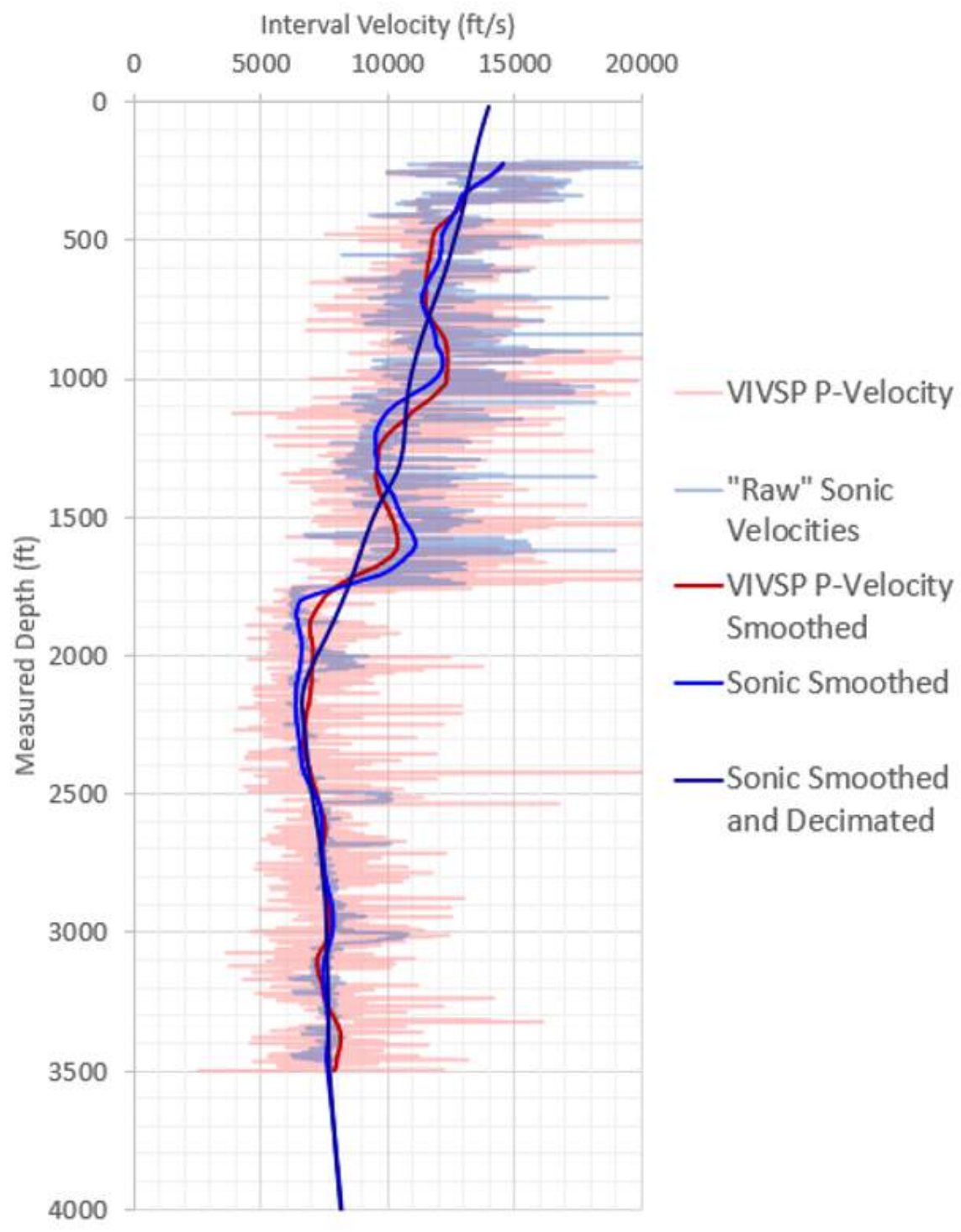
Figure 3.8 Velocity functions used in developing the reverse-time migration (RTM) velocity model: the vertical-incidence vertical seismic profile (VIVSP) estimate (pink), processed sonic logs (light blue), smoothed VIVSP estimates (red), moderately smoothed sonic logs (blue), and heavily smoothed sonic logs (dark blue).
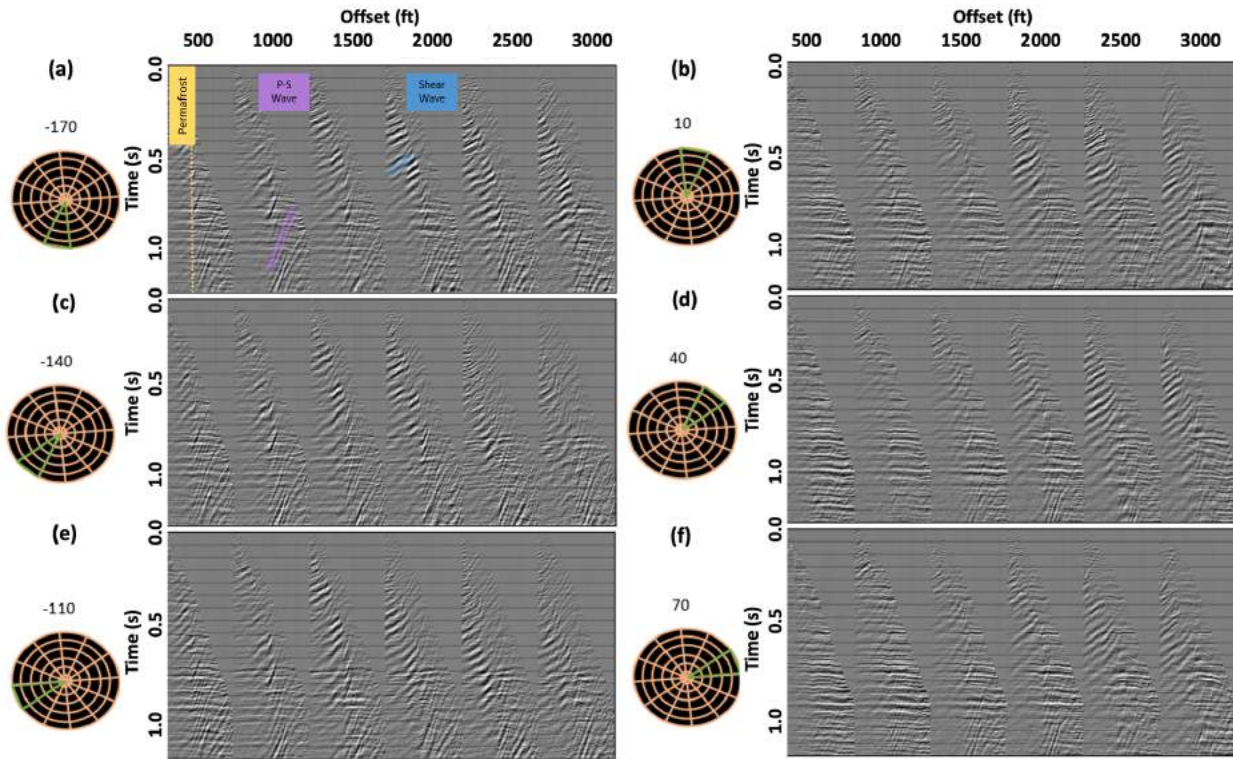
Figure 3.9 Compendium of shot gathers from different offsets and azimuths after applying a reflection-traveltime correction. Each panel has six gathers at different offset ranges where the vertical axis is traveltime and the horizontal axis shows the arrivals at different depths. The presented data are from the following azimuthal bins: (a) -170°, (b) 10°, (c) -140°, (d) 40°, (e) -110°, and (f) 70°. (a) also shows the depth of the base of significant ice-bearing permafrost (yellow) as well as examples of residual S-wave and converted P-S energy.

3.5.2 Common Reflection Point Imaging

The final preprocessing stage involved generating a stacked image cube using the nearly flattened reflection-traveltime-corrected data volume shown in Figure 3.9. To improve the resulting stack quality, we performed a number of prestack filtering operations (windowed bandpass filtering, dip filtering, and applying mild trim statics) on the nearly flattened gathers to improve the overall S/N of the resulting stack. The dip filter has the most significant effect on the final stacked results because it removed most of the otherwise image-contaminating reflected S-wave energy. After applying these steps, we performed common reflection point (CRP) stacking that mapped the traces to their corresponding CRPs within user-specified 50 ft × 50 ft (15 m × 15 m) bin intervals. After CRP stacking, we applied additional post-filtering steps to remove residual noise (i.e., despiking, bandpass and median filtering). Figure 3.10a-b present inline and crossline sections, respectively, through the center of the final 3-D CRP VSP image volume. A benefit of viewing a stacked CRP VSP volume is that it illuminates any reflection point gaps;

however, this also tends to promote an appearance of laterally discontinuous structure. The inline panel (Figure 3.10a) has two distinct blank zones due to the source gaps from the lake (lower left) and the deviation in the well bore (upper right).
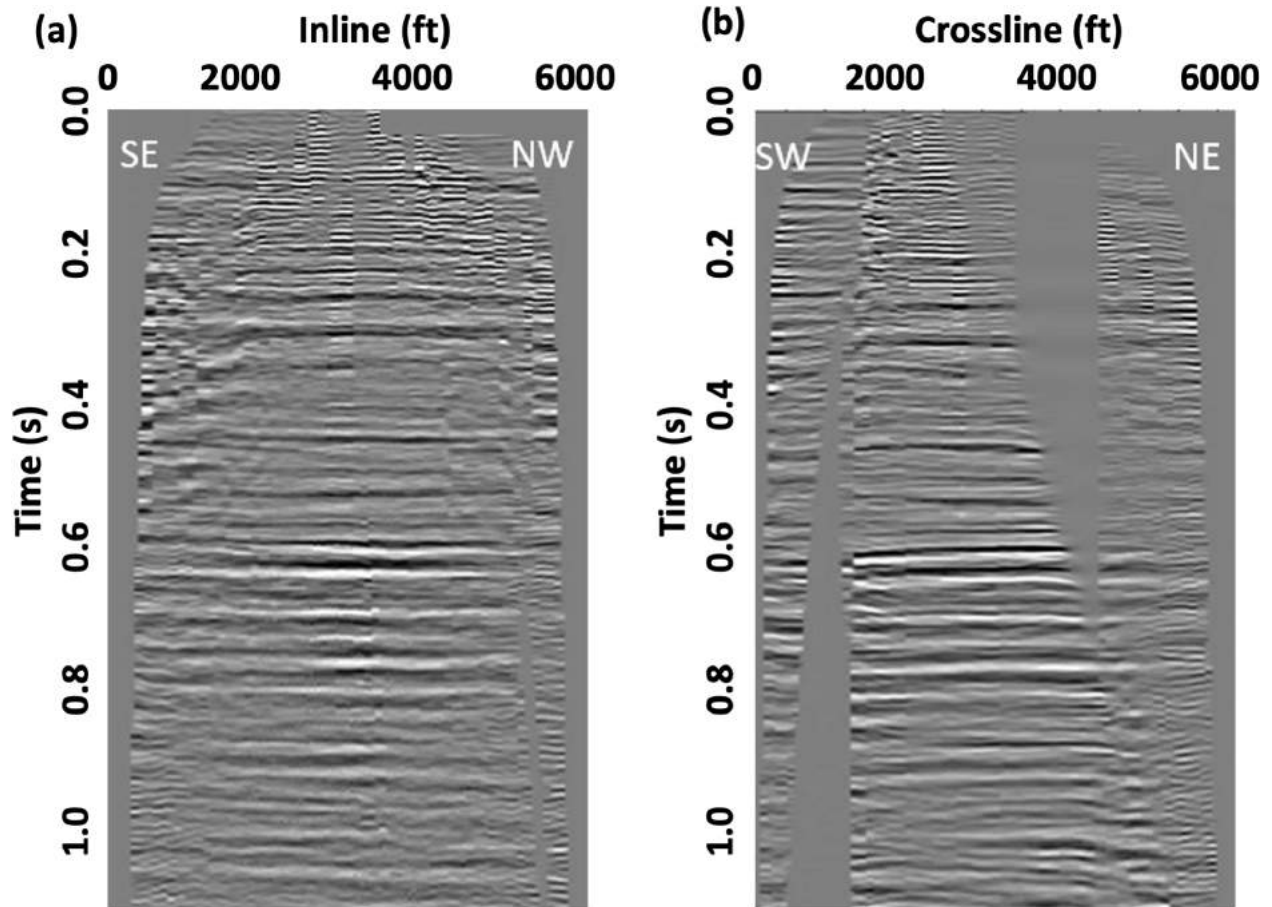
Figure 3.10 (a) Inline and (b) crossline sections from the final common reflection point stacked volume. The sections are extracted from the center of the survey through the wellhead. The noted laterally discontinuous reflections are due to gaps in the surface source coverage (road, lake and pingo) and the well deviations.

3.6   3-D Tomographic Velocity Refinement

The quality of subsurface images generated by prestack wave-equation depth migration algorithms such as VSP RTM highly depends on the accuracy of the 3-D velocity model used for wave propagation [43]. Therefore, building plausible 3-D velocity models remains a key challenge in such imaging applications [44]. Migration velocity analysis is a tool commonly used to generate accurate velocity models and is typically implemented in the image domain [45]. By using the coherency/focusing of prestack common-image gathers, these velocity estimation techniques can successfully update imaging velocities that lead to

37

improved structural images [46]. The method we exploit herein falls into this model-building category and is often referred as image-domain wavefield tomography [47].

Our model building approach is inspired by passive-seismic elastic wavefield transmission tomography where one can formulate an inverse problem to generate accurate P- and S- wave velocity models [48] that optimize the focusing of microseismic source images [49]. One can generate source-event images by using a migration procedure called full-wavefield elastic time-reverse imaging (TRI), which takes the isolated direct P- and S- wavefields recorded at receivers along with a velocity model as input [50]. Similar to the structural imaging algorithms such as RTM, the TRI procedure also requires reliable velocity models to obtain high-quality source images [51].

The DAS 3-D VSP acquisition configuration presented herein allows us to exploit the principle of reciprocity by exchanging the locations of sources and receivers to set up a computationally efficient imaging and tomography problem with the (reciprocal) sources and receivers located at the borehole and surface, respectively. This reciprocal geometry mimics a conventional surface microseismic monitoring investigation where one can conveniently apply a transmission image-domain elastic tomography analysis. In the case of this DAS VSP data set, unlike in a passive seismic experiment, the reciprocal downhole source locations and times are known, allowing further optimization of the tomography algorithm.

Our elastic inversion strategy is based upon a multi-term objective function that measures the focusing of time-reversed energy in zero-lag and extended source images [52]. The objective function applies penalty operators to source images to annihilate well-focused energy and emphasizes poorly focused residual energy arising from the incorrect imaging velocities. Minimizing the objective function using a non-linear gradient-based iterative method [53] optimizes the P- and S-wave velocity model updates that result in improved image focusing. The gradient of the objective function is computed by applying the adjoint-state method [54]. Because one of the main goals herein is to produce structural images generated via acoustic RTM, only the recovered P-wave velocity model is used as an input for the RTM algorithm; however, this analysis also generates an S-wave velocity model for follow-on elastic imaging work if desired.

Our velocity model building strategy includes an initial extrapolation of the 1-D P-wave velocity profile (Figure 3.8) throughout the 3-D model domain. Using the elastic inversion approach, we expect to recover the required spatial velocity variations throughout the model, which would result in improved VSP RTM image quality. Figure 3.11 depicts the recovered 3-D P-wave velocity model (Figure 3.11a) and as a perturbation from the 1-D starting model (Figure 3.11b) after applying ten iterations of the tomographic inversion procedure.
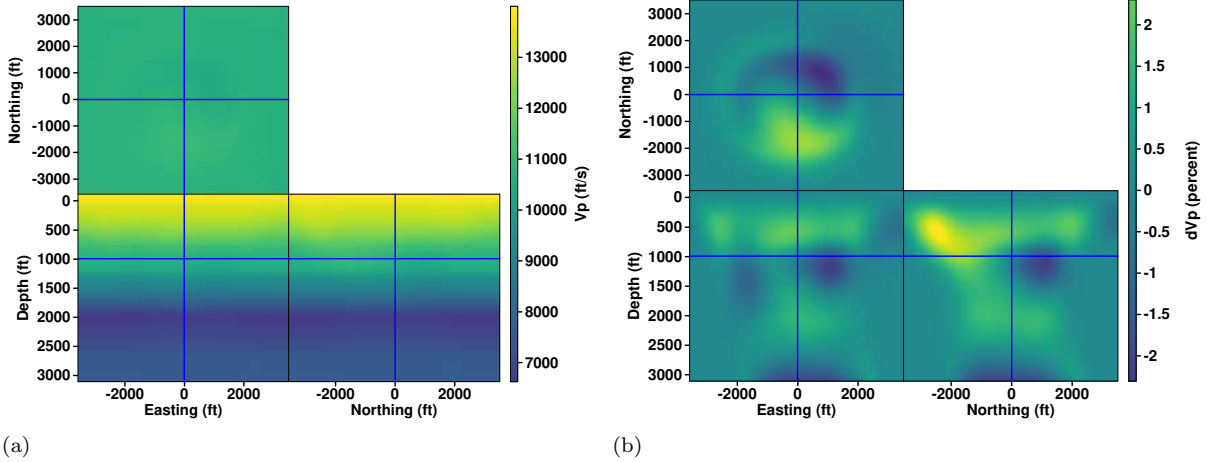
Figure 3.11 Inverted 3-D P-wave velocity model shown as (a) a full volume and (b) as a perturbation from the 1-D reference background model in Figure 3.8. Blue lines in each image panel indicate locations of the other panel.

Within the ice-bearing permafrost zone down to a depth of 1000 ft (305 m), the update largely increases P-wave velocities up to 2.5%, whereas between 1000 ft (305 m) and 1800 ft (549 m) around the BIBPF velocities are largely decreased by -2.5%. Furthermore, the inverted model exhibits increased velocities around the D1 hydrate reservoir at 2294 ft (699 m) depth while negative model updates are required throughout the B1 gas hydrate reservoir level at 2769 ft (844 m). The reason we observe mostly 1-D model updates (minimal lateral heterogeneity) below the ice-bearing permafrost zone is that the aperture angle between reciprocal sources and receivers becomes significantly narrower and becomes more vertically dominated relative to the shallower part of the model.

To initially evaluate the quality of the recovered elastic models, we apply the TRI procedure and estimate the downhole source positions based on the maximum absolute amplitude of the zero-lag imaged sources. As a result of such analysis, we find the average misfit between the true and estimated source positions to be about ±3 ft (1 m), which indicates that the inverted models exhibit a reasonable accuracy for further structural imaging applications.

3.7 3-D RTM Imaging

Prestack depth migration includes a number of different advanced seismic imaging methods that use wavefield information propagated into the subsurface via a wave-equation solver to form an image. Compared to other PSDM methods, 3-D acoustic RTM explicitly solves the 3-D (constant density) acoustic wave equation (AWE)

$$\frac{\partial^2 U}{\partial t^2} = c^2 \left(\frac{\partial^2 U}{\partial x^2} + \frac{\partial^2 U}{\partial y^2} + \frac{\partial^2 U}{\partial z^2} \right), \tag{3.1}$$

where U is the acoustic wavefield, c is velocity, x, y, z are directional dimensions, and t is time. Accordingly, RTM is considered a full-wavefield imaging method and is not based on an underlying approximation such as that used in ray-based Kirchhoff migration. RTM exploits the time-reversal properties of the AWE, meaning that acoustic wavefield solutions can be evolved either causally forward or anticausally backward in time depending on context. RTM is particularly useful for higher-end imaging scenarios involving complex earth models, significant structural dips, and sharp velocity contrasts; however, the gradual improvement in computer hardware, especially general-purpose graphic processing unit (GPU) cards, makes RTM analyses increasingly accessible for application to more general imaging problems and allows for a push toward higher imaging frequencies that can help improve reflector resolution.

The RTM procedure has three fundamental steps. First, a seismic wavelet is injected into an initially quiescent source wavefield $S(\mathbf{x}, t)$ that is recursively numerically propagated forward in time from $t = 0$ s to a maximum recording time $t = T$ s. Herein, we use a finite-difference time-domain AWE solver optimized to run on NVidia V100 GPU hardware. The second step involves using the preprocessed P-wave reflection data to reconstruct a receiver wavefield $R(\mathbf{x}, t)$ that is iteratively propagated in reverse time from time $t = T$ s to $t = 0$ s. The third step involves applying an imaging condition that combines information from the $S(\mathbf{x}, t)$ and $R(\mathbf{x}, t)$ wavefields at each time step in the reconstruction process (second step) to form a single-shot imaging volume. The three-step RTM imaging procedure is then repeated for each shot gather in the data set, with each successive image stacked into the global final image volume.

Due to the high quality and high frequencies associated with this DAS 3-D VSP data set, we performed RTM imaging on a fine grid with $\Delta x = \Delta y = \Delta z = 3.0$ m discretization intervals and a $2.544 \times 2.544 \times 1.920$ km^3 model size, which resulted in a 3-D model domain of $N_z \times N_x \times N_y = 640 \times 848 \times 848$ grid points. Accordingly, we interpolated the P-wave velocity model from the 3-D tomographic refinement discussed above to the 3.0 m grid, which was input with the processed data to our RTM engine. To model the source wavefield we assumed an Ormsby wavelet with [2, 8.5, 100, 150] Hz corner frequencies. Our forward and reverse-time wavefield propagations involved 4000 time steps with a $\Delta t = 0.3$ ms interval which, given the spatial sampling and velocity model values, is sufficient for satisfying the Courant-Friedrichs-Lewy stability criteria. To form the image, we apply a energy normalized imaging condition,

$$I(\mathbf{x}) = \sum_e \sum_t \frac{S(\mathbf{x}, t|e) R(\mathbf{x}, t|e)}{\sqrt{S(\mathbf{x}, t|e)^2} \sqrt{R(\mathbf{x}, t|e)^2} + \epsilon^2}, \tag{3.2}$$

that computes the zero-lag correlation between the source S and receiver R wavefield and normalizes the result by a measure of the energy present in the source and receiver wavefields, which provides better images by partially accounting for irregular illumination. Here, e is the source index, and the stabilization

factor ϵ is introduced to prevent division by zero. Care must be used to choose an ϵ value (usually through trial and error) that improves the spatial amplitude balance of reflectors but does not significantly increase imaging artifacts. The RTM imaging code and associated run-time parameters were all validated on a basic 3-D synthetic model using the same acquisition geometry as the present field data experiment.

The dimensions of the 3-D data volume used for imaging are 1000 time samples at 2.0 ms, 1699 surface source points (c.f. Figure 3.4 for geometry) and 979 downhole receivers at a 3.0 ft (1 m) interval along the well. Given the model dimensions and number of time steps, each individual shot migration took approximately 8 minutes to complete on a single V100 GPU card. To reduce the overall computational effort, we applied the principle of reciprocity discussed above that allowed us to perform 979 separate imaging runs rather than 1699 without applying reciprocity. Moreover, our initial testing showed that RTM images formed by migrating neighboring reciprocal shot gathers were nearly identical and thus we decided to decimate the number of shots to 98 in total. This led to an overall migration runtime of 784 minutes (approximately 13 hours) on a single NVidia V100 GPU card; however, we point out that the RTM effort could be further parallelized by running separate migrations over different shot subsets on multiple GPU resources if available.

Figure 3.12 presents examples of the 100 Hz 3-D acoustic RTM imaging results extracted through the well origin in the inline and crossline directions.
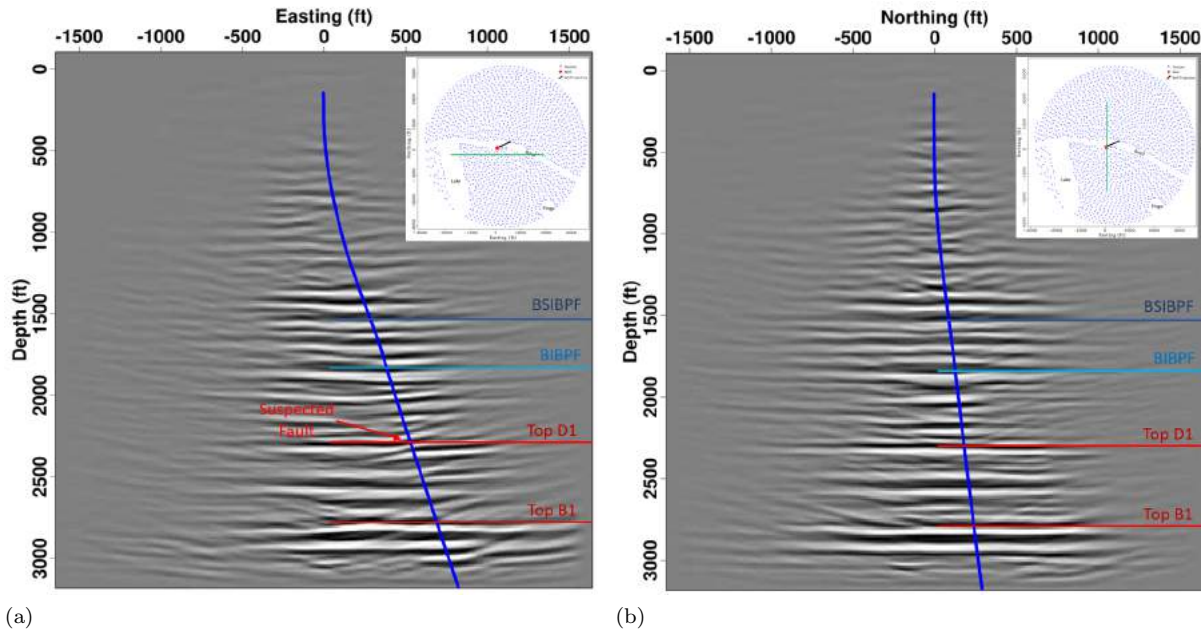
Figure 3.12 100 Hz 3-D acoustic RTM results extracted in the (a) easting and (b) northing planes. The blue curve shows the projected well path through the section. The tops of the B1 and D1 reservoirs are labelled in red, and the base of ice-bearing permafrost and base of significant ice-bearing permafrost are labeled BIBPF and C17, respectively.

We have overlain the well trajectory in these directions with blue lines (note that due to well deviation, the well is as much as 175 ft (51 m) out of the plane of these seismic transects). Overall, the imaging quality is quite high with reflectivity imaged both in and below the ice-bearing permafrost zone. The two horizons of interest, the tops of the D1 and B1 sands at 2294 ft (699 m) and 2769 ft (844 m), respectively, are both clearly imaged as generally horizontal reflectors. We note that the D1 sand reflection in Figure 3.12a appears to be discontinuous to the west of the projected well path, which is consistent with the aforementioned minor fault observed in the Hydrate-01 well-log data. This interpreted fault can be traced through much of the 3-D image volume.

Figure 3.13 presents a comparison between a section of the CRP image after 1-D time-to-depth conversion and a similar section from the 3-D RTM volume. Note that the former image has been converted to depth with the 1-D velocity model shown in Figure 3.8, whereas the RTM image has been migrated through the updated 3-D velocity model. Thus, slight vertical positioning differences between the two images are expected. Overall, similar reflectivity is imaged in both panels. While the CRP image shows somewhat higher frequencies at the target zone locations, it also tends to have more laterally and generally incoherent reflectivity in the ice-bearing permafrost zone. Finally, Figure 3.14 shows the image oriented in the azimuth of the deviated well extracted from the 3-D RTM volume with the V_P log data

42

overlain as a well tie as well as the interpreted key horizons. Overall, we see good well-tie matches at the four indicated key horizons, as well as unlabeled locations within the permafrost zone.

(a)   (b)
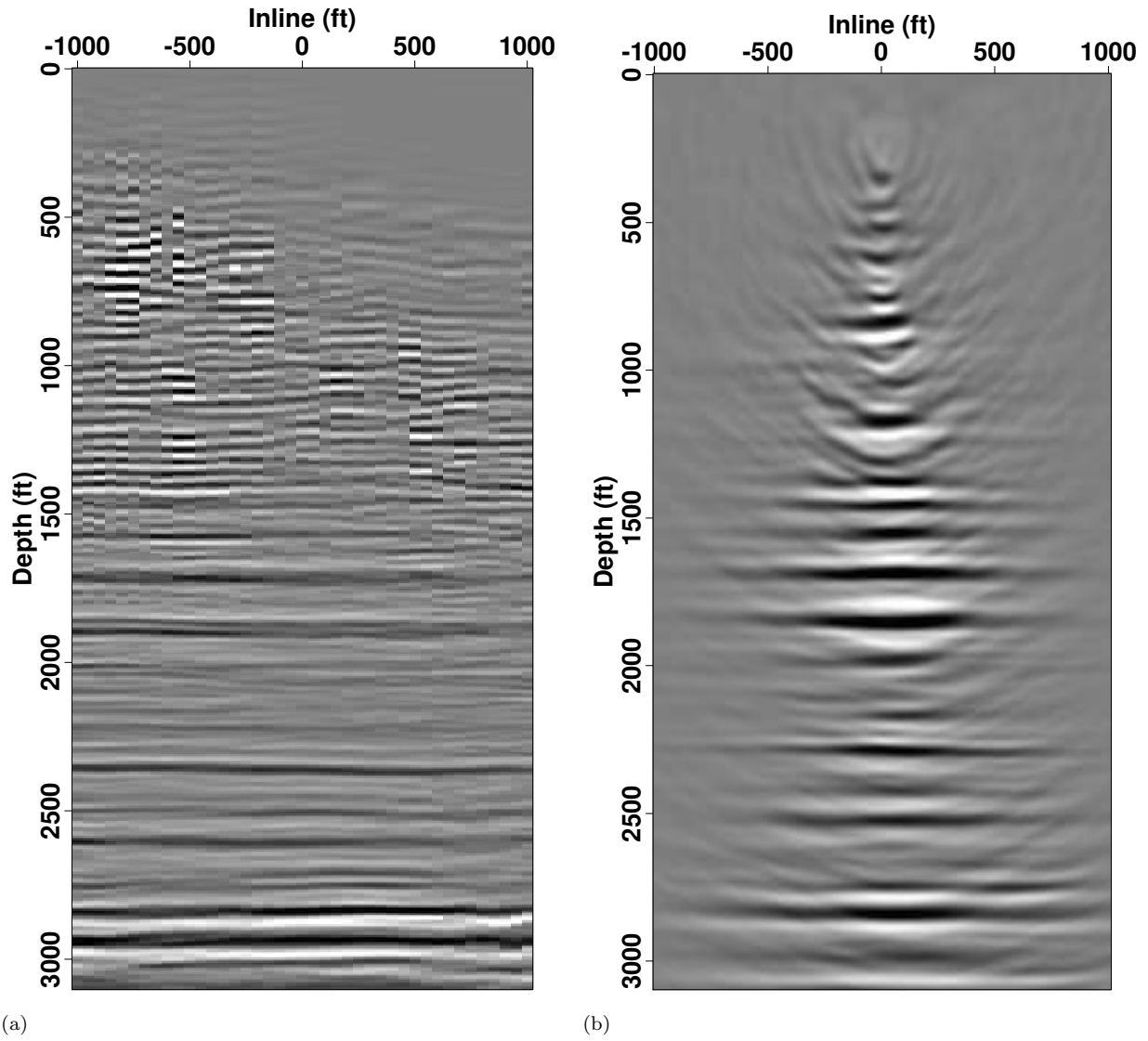
Figure 3.13 (a) Common reflection point stack results after time-to-depth conversion. (b) 100 Hz 3-D acoustic RTM in the easting plane extracted through the well location at the surface.
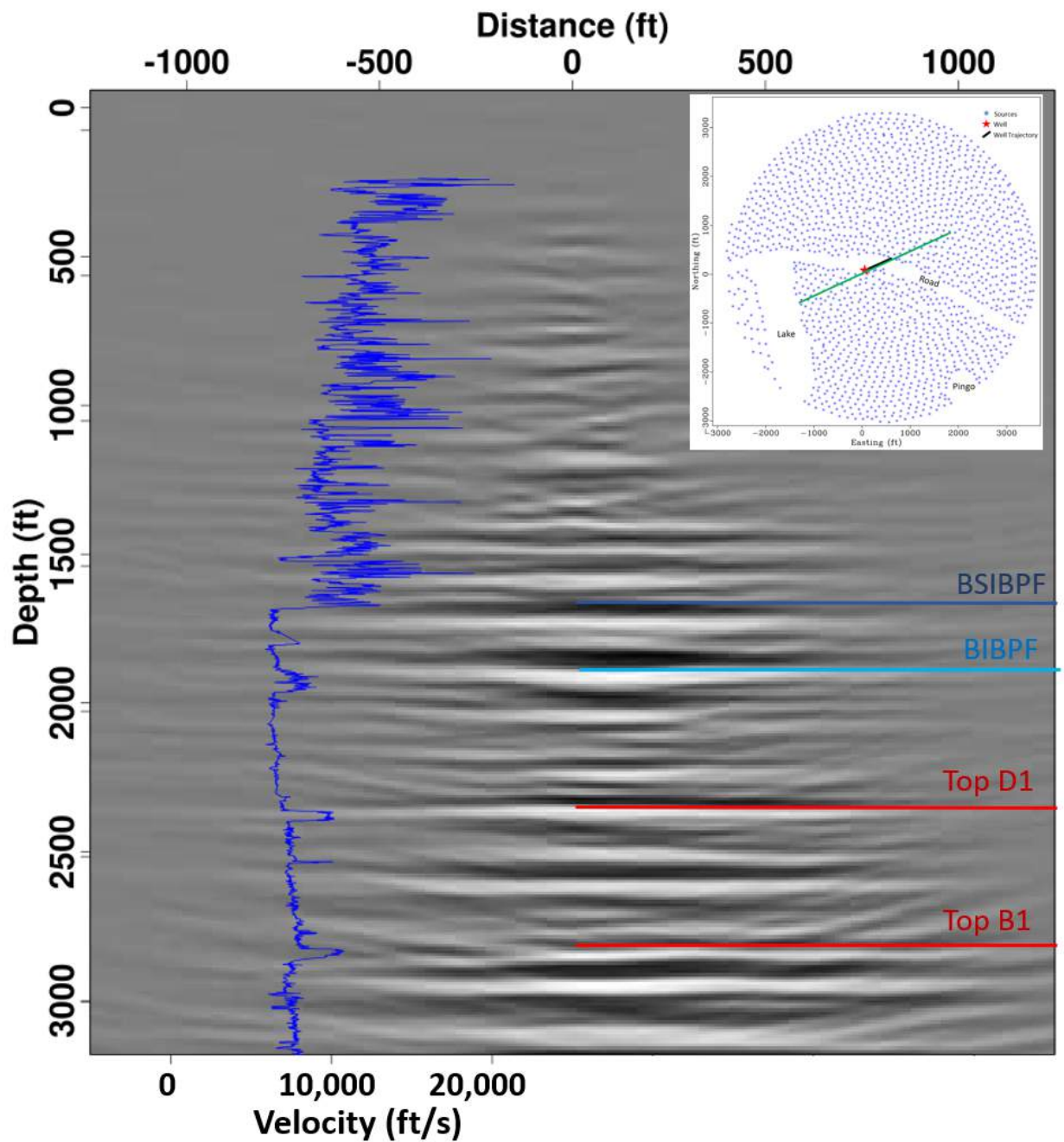
Figure 3.14 100 Hz 3-D acoustic RTM imaging results oriented in the azimuth of the deviated well extracted with the V_P well log shown in blue. The depth of four main interfaces inferred from log data are shown to the right of the image, including the tops of the D1 and B1 sands as well as the base of ice-bearing permafrost (BIBPF) and base of significant ice-bearing permafrost (C17).

3.8 Discussion

The 3-D acoustic RTM analysis applied to the Hydrate-01 DAS 3-D VSP data set generated high-quality imaging results that clearly show the main features of interest and add to our geologic understanding of the site. We can observe the reflections corresponding with the thin-bed D1 and B1 sands as being laterally continuous over the area of data coverage, with relatively consistent reflection amplitude suggesting laterally homogeneous reservoir properties and gas hydrate saturation, both of which are important for production testing. Despite high-frequency data and an imaging approach focused on maintaining resolution, the tops and bottoms of the two sands cannot be clearly distinguished in either the RTM or CRP stack analyses. We also note that horizons appear generally flat and horizontal, fitting with regional trends. In addition, indications of faulting (Figure 3.12) help confirm the location of the previously interpreted fault, and the apparent magnitude of fault slip indicated by the RTM results is consistent with inferences based on other data.

Over the past decade there has been significant research interest in developing 3-D acoustic LSRTM technology [55], which formally recasts RTM as an inverse problem that aims to minimize the effects of incomplete acquisition (e.g., limited offsets, acquisition holes) [56] and recover physical estimates of reflectivity rather than RTM reflector images without calibrated units [57]. By doing so, acoustic LSRTM demonstrably leads to higher-resolution results than their RTM counterparts [58] and potentially leads to a more quantitative interpretation of subsurface reflectivity [59]. An open and interesting question is the degree to which such a 3-D acoustic LSRTM analysis could further improve the RTM images presented herein and potentially help resolve the tops and bottom of key units of interest.

An interesting observation is that the DAS 3-D VSP data volume has remarkably high quality of both P- and S-waves. While S-waves have been effectively treated as unwanted signal in the present 3-D acoustic RTM imaging work, a fully elastic 3-D RTM imaging could be used to generate multiple complementary image volumes including reflected P-P, converted P-S, and reflected S-S. Because S-waves travel more slowly than P-waves, they have shorter wavelengths for a given frequency and thus a S-S (or P-S) image potentially offers higher resolution than a P-P image. A 3-D elastic RTM imaging analysis is currently being undertaken by the project team using the P- and S-wave models jointly inverted through the 3-D elastic image-domain tomography procedure described above.

The move toward higher-resolution images likely would be assisted by performing a 3-D elastic full-waveform inversion (E-FWI) analysis. Unlike the 3-D elastic image-domain tomography applied herein, E-FWI aims to match waveforms in the data domain and thus represents the most stringent test for elastic model building techniques to pass. However, a successful E-FWI analysis could generate a significantly

higher-resolution velocity model that could lead to further imaging and resolution improvements for resolving the thin hydrate units, especially when coupled with an elastic LSRTM approach [60].

3.9   Conclusions

This study presented and applied a seismic processing and depth imaging workflow using a large-scale DAS 3-D VSP data set with the aim of creating optimal seismic images to be used in improving our understanding of the geology in the vicinity of the stratigraphic test well drilled in the Prudhoe Bay Unit area of the North Slope of Alaska. Given high-quality DAS data, our preprocessing efforts successfully separated upgoing reflected P-wave signal from the downgoing and/or S-wave wavefield contributions, which led to a largely noise-free data set that is well conditioned for 3-D RTM analysis.

The petrophysical log data acquired at the stratigraphic test well provided a reasonable starting model for CRP stack analysis; however, residual moveouts in the reflection-traveltime-corrected domain suggested that additional 3-D velocity model refinement was necessary. Based on an analogy with microseismic imaging scenarios, we applied 3-D elastic image-domain tomography to estimate 3-D perturbations from the 1-D background model on the order of $\pm 2.5\%$. The resulting 3-D acoustic RTM images based on estimated 3-D P-wave velocity model showed interpretable reflectivity within and below the ice-bearing permafrost zone, including the D1 and B1 sand reservoirs within the D and B units as well as minor faulting, that matches log data in well-ties. Finally, while this imaging approach generated high-quality imaging results, future work with acoustic or elastic LSRTM may lead to higher-resolution results and lead to more quantitative interpretations of subsurface properties.

CHAPTER 4

CONCLUSIONS AND FUTURE WORK

Developments in DAS interrogator technology the deployment of optical fiber in VSP surveys have motivated the development of a seismic imaging framework that can improve seismic image quality and resolution and is flexible to different DAS 3-D VSP investigations. The high spatial and temporal measurement density afforded by DAS 3-D VSP acquisition provides an opportunity for recording high-quality, high-frequency, and finely sampled P- and S- wavefields. The high-quality and high-frequency DAS data opens up the possibility of generating seismic images using high-frequency 3-D reverse-time migration. This imaging technology serves as a powerful high-end imaging framework because it can generate high-resolution images involving complex earth models, significant structural dips, and sharp velocity contrasts.

To establish the RTM image procedure, a FD modeling code was developed to solve the acoustic wave equation, and code validation done with a synthetic velocity model and source wavelet. An temporal 2nd-order and spatial 8th-order FD stencil was used to define the FDTD solver to calculate forward and reverse wavefield propagation. A 100 Hz Ormsby wavelet was used to represent the source wavelet produced from correlated Vibroseis data, and used in the source wavefield propagation. LWD data were used to generate an initial 3-D velocity model for input into the RTM code. During the validation of the RTM procedure, comparisons between different imaging conditions were made in terms of amplitude balancing and resolution of the final image volume, which led to the selection of a energy normalized imaging condition for the imaging work reported in this thesis.

Following the development and testing of the CUDA-based RTM code on controlled tests using synthetic models, I applied the validated 3-D RTM code to an Alaskan DAS 3-D VSP data set to generate image volumes for ensuing geologic interpretations. Tests with different imaging conditions on field data similarly demonstrated that the energy normalized imaging condition approach provided better model illumination and higher-resolution seismic images. Challenges faced during the 3-D RTM code development and application included handling of the high-frequency data content, the irregular surface source geometry and topography, and the moderate borehole deviation. The high frequencies required using a finely spaced velocity model and small propagation time steps due to stability considerations. The surface elevation has slight variations; however, the scale of these variations is near the same as the grid size, allowing for a level-surface approximation. Finally, I accounted for borehole deviation using an inverse-distance weighting method to scale the data injection at neighboring locations within the wavefield volume.

Use the 3-D RTM framework, I generated a seismic image volume and extracted 2-D image lines for visualization purposes. Overall, the image quality is high with highly resolved reflectivity observed throughout the model at locations expected from the source-receiver migration aperture. Applying a post-migration velocity-dip filter proved necessary, though, to remove most steeply dipping migration swing artifacts. Four key horizons of interest are clearly imaged in the RTM results, including the two target hydrate reservoirs. Observations show that the reflections corresponding with the thin-bed D1 and B1 sands are laterally continuous over the area of data coverage, with consistent reflection amplitude suggesting laterally homogeneous reservoir properties and gas hydrate saturation. In addition, a potential discontinuity is noted to the west of the projected well trajectory near the top of the D1 sand reflection, which is an consistent with background geologic information and important for future project planning in terms of well placement and gas-hydrate production testing. An image cross-section extracted along the orientation of the deviated well trajectory was used to perform a well-tie analysis to confirm the depths of the four key horizons.

4.1 Future Work

The produced image volume is high quality with the reservoir units clearly distinguishable. However, improvements to the final image volume are desired to provide information ideally for both the reservoir tops and bottoms, as well as obtaining quantitative information on subsurface reflectivity. To do this, there is research interest to expand on the 3D acoustic RTM imaging procedure using three imaging techniques: (1) acoustic least-squares RTM (LSRT); (2) elastic RTM and elastic LSRTM; and (3) elastic FWI.

The DAS 3-D VSP data set had surface acquisition gaps due to preexisting environmental features, and produced an image volume with clear reflectivity, but provided no physical estimates of reflectivity values. Acoustic LSRTM could solve these issues by formulating the RTM procedure into an inverse problem. This approach would help address the deleterious effects of incomplete acquisition and recover physical estimates of reflectivity information. Additionally, such an analysis would lead to higher-resolution images and allow for a more quantitative interpretation to be conducted.

The acoustic RTM procedure described in this thesis used the preprocessed P- wavefield data; however, the full DAS 3-D VSP data set contained high-quality P- and S- wavefield information. Having access to both wavefield data, an expansion in RTM imaging procedure could be made from acoustic imaging to elastic imaging for both RTM and LSRTM. This fully elastic imaging would generate 3-D image volumes that could be used for a more complete gas-hydrate reservoir characterization. Furthermore, because S-waves have shorter wavelengths compared to their P-wave counterparts, they potentially could offer even higher-resolution images compared to the acoustic P-wave imaging approach.

Lastly, elastic imaging can be pushed further with the use of elastic FWI. The aim of this procedure would be to match waveforms in the data domain, which represents the most stringent test for elastic model building[61]. If successful it can generate an even higher-resolution velocity model and the associated imaging improvements, especially when combined with an elastic LSRTM method.

REFERENCES

[1] A. Kumar, E. Zorn, R. Hammack, and W. Harbert. Surface Seismic Monitoring of Hydraulic Fracturing Activity in Pennsylvania and West Virginia. *Unconventional Resources Technology Conference Proceedings*, page 2435574, 2016.

[2] A. Mendecki, G. Aswegen, and P. Mountfort. A guide to routine seismic monitoring in mines. *A Handbook on Rock Engineering Practice for Tabular Hard Rock Mines, Edition: 1 Chapter: A guide to routine seismic monitoring in mines, The Safety in Mines Research Advisory Committee*, 1999.

[3] D. Lumley. 4D seismic monitoring of CO2 sequestration. *The Leading Edge*, 29(2):150–155, 2010.

[4] J. Mestayer, B. Cox, P. Wills, D. Kiyashchenko, J. Lopez, M. Costello, S. Bourne, G. Ugueto, R. Lupton, G. Solano, D. Hill, and A. Lewis. Field Trials of Distributed Acoustic Sensing for Geophysical Monitoring. *SEG Technical Program Expanded Abstracts*, pages 4253–4257, 2011.

[5] A. Mateeva, J. Lopez, J. Mestayer, P. Wills, B. Cox, D. Kiyashchenko, Z. Yang, R. Detomo, and S. Grandi. Distributed acoustic sensing for reservoir monitoring with VSP. *The Leading Edge*, 32(10): 1278–1283, 2013.

[6] T. Daley. Field testing of fiber-optic distributed acoustic sensing (DAS) for subsurface seismic monitoring. *The Leading Edge*, 32(6):699–706, 2013.

[7] A. H. Hartog. *An Introduction to Distributed Optical Fibre Sensors*. Taylor & Francis Group, 2018.

[8] Oscar J Ferrians. Permafrost in alaska. *The Geology of North America*, 1:845–854, 1994.

[9] Ge Zhan, Jan Kommedal, and Jay Nahm. Vsp field trials of distributed acoustic sensing in trinidad and gulf of mexico. 2015. doi: 10.1190/segam2015-5876420.1.

[10] A. F. Baird, A. L. Stork, S. A. Horne, G. Naldrett, J.-M. Kendall, J. Wookey, J. P. Verdon, and A. Clarke. Characteristics of microseismic data recorded by distributed acoustic sensing systems in anisotropic media. *Geophysics*, 85(4):KS139–KS147, 2020.

[11] S. Cole, M. Karrenbach, D. Kahn, J. Rich, K. Silver, and D. Langton. Source parameter estimation from das microseismic data. pages 4928–4932, 2018.

[12] K. Hornman, B. Kuvshinov, P. Zwartjes, and A. Franzen. Field trial of a broadside-sensitive distributed acoustic sensing cable for surface seismic. *Conference Proceedings, 75th EAGE Conference & Exhibition incorporating SPE EUROPEC 2013*, 2013.

[13] E. Baysal, D. Kosloff, and J. Sherwood. Reverse Time Migration. *Geophysics*, 48(11):1514–1524, 1983.

[14] J. Cabezas, M. Araya, I. Gelado, N. Navarro, E. Morancho, and J. Cela. High-Performance reverse time migration on GPU. *2009 International Conference of the Chilean Computer Science Society*, 2009. doi: 10.1109/SCCC.2009.19.

[15] Denis Kiyashchenko, Albena Mateeva, Yuting Duan, Duane Johnson, Jonathan Pugh, Axel Geisslinger, and Jorge Lopez. Frequent 4d monitoring with das 3d vsp in deep water to reveal injected water-sweep dynamics. *The Leading Edge*, 39(7):471–479, 2020. doi: 10.1190/tle39070471.1.

[16] C. Young, J. Shragge, W. Schultz, S. Haines, C. Oren, J. Simmons, and T. Collett. Advanced Distributed Acoustic Sensing Vertical Seismic Profile Imaging of an Alaska North Slope Gas Hydrate Field. *Energy & Fuels*, 36(6), 2022. doi: 10.1021/acs.energyfuels.1c04102.

[17] F. Audebert, D. Nichols, T. Rekdal, B. Biondi, D. Lumley, and H. Urdaneta. Imaging complex geologic structure with single-arrival Kirchhoff prestack depth migration. *Geophysics*, 62(5):1533–1543, 1997.

[18] R. Hill. Prestack Gaussian-beam depth migration. *Geophysics*, 66(4):1240–1250, 2001.

[19] A. Valenciano and B. Biondi. 2-D deconvolution imaging condition for shot-profile migration. *SEG Technical Program Expanded Abstracts*, pages 1059–1062, 2003.

[20] R. Courant, K. Friedrich, and H. Lewy. *On the Partial Difference Equations of Mathematical Physics*. IBM, 1967.

[21] L. Knopoff and A. Gangi. Seismic Reciprocity. *Geophysics*, 24(4):681–691, 1959.

[22] Schlumberger. Petrel E&P Software, 2021.

[23] O Yilmaz. *Seismic Data Analysis*. Society of Exploration Geophysicists, 2001.

[24] Y. Kim, D. Min, and C. Shin. Frequency-domain reverse time migration with source estimation. *Geophysics*, 76(2):S41–S49, 2011.

[25] T. Collett, A. Johnson, C. Knapp, and R. Boswell. *Natural Gas Hydrates - Energy Resource Potential and Associated Geologic Hazards Volume 89*. American Association of Petroleum Geologists, 2009.

[26] R. Boswell, S. Hancock, K. Yamamoto, T. Collett, M. Pratap, and S.-R. Lee. *Natural gas hydrates: Status of potential as an energy resource: Chapter 6 in "Future Energy"*. USGS Publications Warehouse, 2020.

[27] T. Inks, M. Lee, W. Agena, D. Taylor, T. Collett, M. Zyianova, and R. Hunter. Seismic Prospecting for gas hydrate and associated free-gas prospects in the Milne Point Area of Northern Alaska. *Natural Gas Hydrates – Energy Resource Potential and Associated Geologic Hazards: American Association of Petroleum Geologists Memoir*, 89:14, 2009.

[28] R. Boswell, S. Bünz, T. Collett, M. Frye, T. Fujii, D. McConnell, J. Meinert, I. Pecher, T. Reichel, B.-J. Ryu, J. Shelander, D. Shelander, and K. Shin. Introduction to special section: Exploration and characterization of gas hydrates. *Interpretation*, 4(1):SAi–SAii, 2016.

[29] M. Karrenbach, S. Cole, A. Ridge, K. Boone, D. Kahn, J. Rich, K. Silver, and D. Langton. Fiber-optic distributed acoustic sensing of microseismicity, strain, and temperature during hydraulic fracturing. *Geophysics*, 84(1):D11–D23, 2019.

[30] R. Boswell, T. Collett, N. Okinaka, R. Hunter, K. Suzuki, M. Tamaki, J. Yoneda, S. Haines, D. Itter, E. Myshakin, and G. Moridis. Alaska North Slope Hydrate-01 Stratigraphic Test Well program: Technical Results. *Energy & Fuels*, 36(6):doi:10.1021/acs.energyfuels.2c00327, 2022.

[31] T.S. Collett. Natural gas hydrates of the Prudhoe Bay and Kuparuk River area, North Slope, Alaska. *American Association of Petroleum Geologists Bulletin*, 77(5):793–812, 1993.

[32] M. Tamaki, A. Fujimoto, R. Boswell, and T. Collett. Geological reservoir characterization of a gas hydrate prospect associate with the Hydrate-01 stratigraphic test well, Alaska North Slope. *Energy & Fuels*, 36(6):doi:10.1021/acs.energyfuels.2c03369, 2022.

[33] R. Hunter, T. Collett, R. Boswell, B. Anderson, S. Digert, G. Pospisil, R. Baker, and M. Weeks. Mount Elbert Gas Hydrate Stratigraphic Test Well, Alaska North Slope: Overview of scientific and technical program. *Marine and Petroleum Geology*, 28(2):295–310, 2011.

[34] R. Boswell, K. Rose, T. Collett, M. Lee, W. Winters, K. Lewis, and W. Agena. Geologic controls on gas hydrate occurrence in the Mount Elbert prospect, Alaska North Slope. *Marine and Petroleum Geology*, 28(2):589–607, 2011.

[35] T. Collett, R. Boswell, M. Lee, B. Anderson, K. Rose, and K. Lewis. Evaluation of long-term gas hydrate production testing locations on the Alaska North Slope. *SPE Reservoir Evaluation and Engineering*, 15(2):243–264, 2012.

[36] W. Winters, M. Walker, R. Hunter, T. Collett, R. Boswell, K. Rose, W. Waite, M. Torres, S. Patil, and A. Dandekar. Physical properties of sediment from the Mount Elbert Gas Hydrate Stratigraphic Test Well, Alaska North Slope. *Marine and Petroleum Geology*, 28(2):361–380, 2011.

[37] T. Collett, M. Zyrianova, N. Okinaka, M. Wakatsuki, R. Boswell, S. Marsteller, D. Minge, S. Crumley, D. Itter, R. Hunter, A. Garcia-Ceballos, and G Jin. Design and operations of the Hydrate-01 stratigraphic test well, Prudhoe Bay Unit, Alaska North Slope. *Energy & Fuels*, 36(6): doi:10.1021/acs.energyfuels.1c04087, 2022.

[38] T. Lim, A. Fujimoto, and T. Kobayashi. DAS 3D VSP data acquisition at 2018 Stratigraphic Test Well (Hydrate-01). *Proc. ICGH-10, Singapore*, 2020.

[39] A. Fujimoto, T. Lim, M. Tamaki, K. Kawaguchi, T. Kobayashi, S. Haines, T. Collett, and R. Boswell. DAS 3D VSP survey at Stratigraphic Test Well (Hydrate-01). *SEGJ International Symposium*, 2021.

[40] Shearwater GeoServices. Shearwater Reveal, 2021.

[41] Landmark Solutions. SeisSpace, 2021.

[42] J. Zhang and Z. Zhang. Application of successive approximation method to the computation of the Green's function in axisymmetric inhomogeneous media. *IEEE Transactions on Geoscience and Remote Sensing*, 36:732–737, 1998.

[43] S. Gray, J. Etgen, J. Dellinger, and D. Whitmore. Seismic migration problems and solutions. *Geophysics*, 66(5):1622–1640, 2001.

[44] J. Etgen, S.H. Gray, and Y. Zhang. An overview of depth imaging in exploration geophysics. *Geophysics*, 74:WCA5–WCA17, 2009.

[45] K. Al-Yahya. Velocity analysis by iterative profile migration. *Geophysics*, 54(6):718–729, 1989.

[46] W. Symes. Migration velocity analysis and waveform inversion. *Geophysical Prospecting*, 56(6): 765–790, 2008.

[47] T. Yang and P. Sava. Image-domain wavefield tomography with extended common-image-point gathers. *Geophysical Prospecting*, 63(5):1086–1096, doi:10.1111/1365–2478.12204, 2015. ISSN 13652478.

[48] B. Witten and J. Shragge. Image-domain velocity inversion and event location for microseismic monitoring. *Geophysics*, 82(5):KS71–KS83, 2017.

[49] C. Oren and J. Shragge. Image-domain elastic wavefield tomography for passive data. *90th Annual International Meeting, SEG, Expanded Abstracts*, pages 3669–3673, 2020.

[50] B. Witten and J. Shragge. Extended wave-equation imaging conditions for passive seismic data. *Geophysics*, 80(6):WC61–WC72, 2015.

[51] C. Oren and J. Shragge. PS energy imaging condition for microseismic data – Part 1: Theory and applications in 3D isotropic media. *Geophysics*, 86(2):KS37–KS48, 2021.

[52] C[an] Oren and J[effrey] Shragge. Passive-seismic image-domain elastic wavefield tomography. *Geophysical Journal International*, 228:1512–1529, 2022.

[53] J. Nocedal and S. Wright. *Numerical optimization.* Springer Science and Business Media, 2006.

[54] R.-E. Plessix. A review of the adjoint-state method for computing the gradient of a functional with geophysical applications. *Geophysical Journal International*, 167:495–503, 2006.

[55] M. Wong, S. Ronen, and B. Biondi. Least-squares reverse time migration/inversion for ocean bottom data: A case study. *SEG Technical Program Expanded Abstracts 2011, Society of Exploration Geophysicists*, pages 2369–2373, 2011.

[56] W. Dai and G. Schuster. Plane-wave least-squares reverse-time migration. *Geophysics*, 78(4): S165–S177, 2013.

[57] Y. Zhang, L. Duan, and Y. Xie. A stable and practical implementation of least-squares reverse time migration. *Geophysics*, 80(1):V23–V31, 2015.

[58] C Zeng, S Dong, and B Wang. Adaptive least-squares RTM with applications to subsalt imaging. *Leading Edge*, 35(3):253–257, 2016.

[59] G. Yao and H. Jakubowicz. Least-squares reverse-time migration in a matrix-based formulation. *Geophysical Prospecting*, 64(3):611–621, 2016.

[60] D. Rocha and P. Sava. Elastic least-squares reverse time migration using the energy norm. *Geophysics*, 83(3):S237–S248, 2018.

[61] Anton Egorov, Roman Pevzner, Andrej Bóna, Stanislav Glubokovskikh, Vladimir Puzyrev, Konstantin Tertyshnikov, and Boris Gurevich. Time-lapse full waveform inversion of vertical seismic profile data: Workflow and application to the co2crc otway project. *Geophysical Research Letters*, 44 (14):7211–7218, 2017. doi: https://doi.org/10.1002/2017GL074122.

APPENDIX A

PUBLICATION PERMISSION

This appendix includes the copyright permissions from *Energy & Fuels* (Figure A.1) and (Figure A.2) for use of published papers incorporated as chapters in this thesis.

Reuse/Republication of the Entire Work in Theses or Collections: Authors may reuse all or part of the Submitted, Accepted or Published Work in a thesis or dissertation that the author writes and is required to submit to satisfy the criteria of degree-granting institutions. Such reuse is permitted subject to the ACS' "Ethical Guidelines to Publication of Chemical Research" (http://pubs.acs.org/page/policy/ethics/index.html); the author should secure written confirmation (via letter or email) from the respective ACS journal editor(s) to avoid potential conflicts with journal prior publication*/embargo policies. Appropriate citation of the Published Work must be made. If the thesis or dissertation to be published is in electronic format, a direct link to the Published Work must also be included using the ACS Articles on Request author-directed link − see http://pubs.acs.org/page/policy/articlesonrequest/index.html

* Prior publication policies of ACS journals are posted on the ACS website at
http://pubs.acs.org/page/policy/prior/index.html

Figure A.1 A screenshot granting permission from the American Chemical Society

Figure A.2 A screenshot granting permission from Rightslink by the American Chemical Society

APPENDIX B

AUTHOR AND PROJECT CONTRIBUTION